

Sparse Quantized Spectral Clustering

Zhenyu Liao

ICSI and Department of Statistics
University of California, Berkeley, USA
zhenyu.liao@berkeley.edu

Romain Couillet

G-STATS Data Science Chair, GIPSA-lab
University Grenoble-Alpes, France
romain.couillet@gipsa-lab.grenoble-inp.fr

Michael W. Mahoney

ICSI and Department of Statistics
University of California, Berkeley, USA
mmahoney@stat.berkeley.edu

October 6, 2020

Abstract

Given a large data matrix, sparsifying, quantizing, and/or performing other entry-wise nonlinear operations can have numerous benefits, ranging from speeding up iterative algorithms for core numerical linear algebra problems to providing nonlinear filters to design state-of-the-art neural network models. Here, we exploit tools from random matrix theory to make precise statements about how the eigenspectrum of a matrix changes under such nonlinear transformations. In particular, we show that very little change occurs in the informative eigenstructure even under drastic sparsification/quantization, and consequently that very little downstream performance loss occurs with very aggressively sparsified or quantized spectral clustering. We illustrate how these results depend on the nonlinearity, we characterize a phase transition beyond which spectral clustering becomes possible, and we show when such nonlinear transformations can introduce spurious non-informative eigenvectors.

1 Introduction

Sparsifying, quantizing, and/or performing other entry-wise nonlinear operations on large matrices can have many benefits. Historically, this has been used to develop iterative algorithms for core numerical linear algebra problems (Achlioptas & McSherry, 2007; Drineas & Zouzias, 2011). More recently, this has been used to design better neural network models (Srivastava et al., 2014; Dong et al., 2019; Shen et al., 2020). A concrete example, amenable to theoretical analysis and ubiquitous in practice, is provided by spectral clustering, which can be solved by retrieving the dominant eigenvectors of $\mathbf{X}^\top \mathbf{X}$, for $\mathbf{X} = [\mathbf{x}_1, \dots, \mathbf{x}_n] \in \mathbb{R}^{p \times n}$ a large data matrix (Von Luxburg, 2007; Mahoney, 2016). When the amount of data n is large, the Gram “kernel” matrix $\mathbf{X}^\top \mathbf{X}$ can be enormous, impractical even to form and leading to computationally unaffordable algorithms. For instance, Lanczos iteration that operates through repeated matrix-vector multiplication suffers from an $O(n^2)$ complexity (Golub & Van Loan, 1996) and quickly becomes burdensome.

One approach to overcoming this limitation is **simple subsampling**: dividing \mathbf{X} into subsamples of size εn , for some $\varepsilon \in (0, 1)$, on which one performs parallel computation, and then recombining. This leads to computational gain, but **at the cost of degraded performance**, since each data point \mathbf{x}_i loses the cumulative effect of comparing to the *whole* dataset. An alternative cost-reduction procedure consists in **uniformly** randomly “zeroing-out” entries from the whole matrix $\mathbf{X}^\top \mathbf{X}$, resulting in a sparse matrix with only an ε fraction of non-zero entries. For spectral clustering, by focusing on the eigenspectrum of the “zeroed-out” matrix, Zarrrouk et al. (2020) showed that the same computational gain can be achieved at the cost of a much less degraded performance: for n/p rather large, almost no degradation is observed down to very small values of ε (e.g., $\varepsilon \approx 2\%$ for $n/p \gtrsim 100$).

Previous efforts showed that **it is often advantageous to perform sparsification/quantization in a data-dependent non-uniform manner, rather than uniformly** (Achlioptas & McSherry, 2007; Drineas & Zouzias, 2011). The focus there, however, is on (the non-asymptotic bound of) the approximation error between the original and the sparsified/quantized matrices. This, however, does *not* provide a direct access to the actual performance for spectral clustering or other downstream tasks of interest, e.g., since the top eigenvectors are known to exhibit a phase transition phenomenon (Baik et al., 2005; Saade et al., 2014). That is, they can behave very differently from those of the original matrix, even if the matrix after treatment is close in operator/Frobenius norm to the original matrix.

Here, we focus on the precise characterization of the eigenstructure of $\mathbf{X}^\top \mathbf{X}$ after entry-wise non-linear transformation such as sparsification or quantization, in the large n, p regime, by **performing simultaneously data-dependent non-uniform sparsification and/or quantization (down to binarization)**. We consider a simple mixture data model with $\mathbf{x} \sim \mathcal{N}(\pm \boldsymbol{\mu}, \mathbf{I}_p)$ and let $\mathbf{K} \equiv f(\mathbf{X}^\top \mathbf{X} / \sqrt{p}) / \sqrt{p}$, where f is an entry-wise thresholding/quantization operator (thereby zeroing-out/quantizing entries of $\mathbf{X}^\top \mathbf{X}$); and we prove that this leads to significantly improved performances, with the same computational cost, in spectral clustering as uniform sparsification, but for a much reduced cost in storage induced by quantization. The only (non-negligible) additional cost arises from the extra need for evaluating each entry of $\mathbf{X}^\top \mathbf{X}$. Our main technical contribution (of independent interest, e.g., for those interested in entry-wise nonlinear transformations of feature matrices) consists in using random matrix theory (RMT) to derive the large n, p asymptotics of the eigenspectrum of \mathbf{K} for a wide range of functions f , and then comparing to previously-established results for uniform subsampling and sparsification in (Zarrrouk et al., 2020). Simulations on real-world data further collaborate our findings.

Our main contributions are the following.

1. We **derive the limiting eigenvalue distribution of \mathbf{K} as $n, p \rightarrow \infty$** (Theorem 1), and we identify:
 - (a) the existence of non-informative isolated eigenvectors of \mathbf{K} for some nonlinear f (Corollary 1);
 - (b) in the absence of such eigenvectors, a phase transition in the dominant eigenvalue-eigenvector $(\hat{\lambda}, \hat{\mathbf{v}})$ pair (Corollary 2): if the signal-to-noise ratio (SNR) $\|\boldsymbol{\mu}\|^2$ exceeds a threshold γ , then $\hat{\lambda}$ becomes isolated and $\hat{\mathbf{v}}$ contains data class-structure information exploitable for clustering; if not, then $\hat{\mathbf{v}}$ contains only noise and is asymptotically *orthogonal* to the class-label vector.
2. Letting f be a sparsification, quantization, or binarization operator, we show:
 - (a) a selective sparsification operator, such that $\mathbf{X}^\top \mathbf{X}$ can be drastically sparsified with very little degradation in clustering performance (Proposition 1 and Section 4.2), significantly outperforms the random uniform sparsification in (Zarrrouk et al., 2020);

- (b) for a given matrix storage budget (i.e., fixed number of bits to store \mathbf{K}), an optimal design of the quantization/binarization operators (Proposition 2 and Section 4.3), the performances of which are compared against the original $\mathbf{X}^\top \mathbf{X}$ and its sparsified but not quantized version.

For spectral clustering, **the surprisingly small performance drop, accompanied by a huge reduction in computational cost, contributes to improved algorithms for large problems.** More generally, our proposed analysis sheds light on the effect of entry-wise nonlinear transformations on the eigenspectra of data/feature matrices. Thus, looking forward (and perhaps more importantly, given the use of nonlinear transformations in designing modern neural network models as well as the recent interest in applying RMT to neural network analyses (Li & Nguyen, 2018; Seddik et al., 2018; Jacot et al., 2019; Liu & Dobriban, 2019)), we expect that our analysis opens the door to improved analysis of computationally efficient methods for large dimensional machine learning and neural network models more generally.

2 System model and preliminaries

Basic setup. Let $\mathbf{x}_1, \dots, \mathbf{x}_n \in \mathbb{R}^p$ be independently drawn (non-necessarily uniformly) from:

$$\mathcal{C}_1 : \mathbf{x}_i = -\boldsymbol{\mu} + \mathbf{z}_i, \quad \mathcal{C}_2 : \mathbf{x}_i = +\boldsymbol{\mu} + \mathbf{z}_i \quad (1)$$

with $\mathbf{z}_i \in \mathbb{R}^p$ having i.i.d. zero-mean, unit-variance, κ -kurtosis, sub-exponential entries, $\boldsymbol{\mu} \in \mathbb{R}^p$ such that $\|\boldsymbol{\mu}\|^2 \rightarrow \rho \geq 0$ as $p \rightarrow \infty$, and $\mathbf{v} \in \{\pm 1\}^n$ with $[\mathbf{v}]_i = -1$ for $\mathbf{x}_i \in \mathcal{C}_1$ and $+1$ for $\mathbf{x}_i \in \mathcal{C}_2$.¹ The data matrix $\mathbf{X} = [\mathbf{x}_1, \dots, \mathbf{x}_n] \in \mathbb{R}^{p \times n}$ can be compactly written as $\mathbf{X} = \mathbf{Z} + \boldsymbol{\mu} \mathbf{v}^\top$ for $\mathbf{Z} = [\mathbf{z}_1, \dots, \mathbf{z}_n]$ so that $\|\mathbf{v}\| = \sqrt{n}$ and both $\mathbf{Z}, \boldsymbol{\mu} \mathbf{v}^\top$ have operator norm of order $O(\sqrt{p})$ in the $n \sim p$ regime. In this setting, the Gram (or *linear* kernel) matrix $\mathbf{X}^\top \mathbf{X}$ achieves optimal clustering performance on the mixture model (1); see Remark 1 below. However, it consists of a dense $n \times n$ matrix, which becomes quickly expensive to store or to perform computation on, as n increases.

Thus, we consider instead the following *entry-wise nonlinear* transformation of $\mathbf{X}^\top \mathbf{X}$:

$$\mathbf{K} = \left\{ \delta_{i \neq j} f(\mathbf{x}_i^\top \mathbf{x}_j / \sqrt{p}) / \sqrt{p} \right\}_{i,j=1}^n \quad (2)$$

for $f : \mathbb{R} \rightarrow \mathbb{R}$ satisfying some regularity conditions (see Assumption 1 below), where $\delta_{i \neq j}$ equals 1 for $i \neq j$ and equals 0 otherwise. The diagonal elements $f(\mathbf{x}_i^\top \mathbf{x}_i / \sqrt{p})$ (i) bring no additional information for clustering and (ii) do not scale properly for p large ($\mathbf{x}_i^\top \mathbf{x}_i / \sqrt{p} = O(\sqrt{p})$). Thus, following (El Karoui, 2010; Cheng & Singer, 2013), they are discarded.

Most of our technical results hold for rather generic functions f , e.g., those of interest beyond sparse quantized spectral clustering, but we are particularly interested in f with nontrivial numerical properties (e.g., promoting quantization and sparsity):

$$\textbf{Sparsification:} \quad f_1(t) = t \cdot 1_{|t| > \sqrt{2}s} \quad (3)$$

$$\textbf{Quantization:} \quad f_2(t) = 2^{2-M} (\lfloor t \cdot 2^{M-2} / \sqrt{2}s \rfloor + 1/2) \cdot 1_{|t| \leq \sqrt{2}s} + \text{sign}(t) \cdot 1_{|t| > \sqrt{2}s} \quad (4)$$

$$\textbf{Binarization:} \quad f_3(t) = \text{sign}(t) \cdot 1_{|t| > \sqrt{2}s} \quad (5)$$

Here, $s \geq 0$ is some *truncation threshold*, and $M \geq 2$ is a number of information bits.² The visual representations of these f s are given in Figure 1-(left). For f_3 , taking $s \rightarrow 0$ leads to the sign function $\text{sign}(t)$. In terms of storage, the quantization f_2 consumes $2^{M-2} + 1$ bits per non-zero entry, while the binarization f_3 takes values in $\{\pm 1, 0\}$ and thus consumes 1 bit per non-zero entry.

¹The norm $\|\cdot\|$ is the Euclidean norm for vectors and the operator norm for matrices.

²Also, here, $\lfloor \cdot \rfloor$ denotes the floor function, while $\text{erf}(x) = \frac{2}{\sqrt{\pi}} \int_0^x e^{-t^2} dt$ and $\text{erfc}(x) = 1 - \text{erf}(x)$ denotes the error function and complementary error function, respectively.

Random matrix theory. To provide a precise description of the eigenspectrum of \mathbf{K} for the nonlinear f of interest, to be used in the context of spectral clustering, we will provide a large dimensional characterization for the *resolvent* of \mathbf{K} , defined for $z \in \mathbb{C} \setminus \mathbb{R}^+$ as

$$\mathbf{Q}(z) \equiv (\mathbf{K} - z\mathbf{I}_n)^{-1}. \quad (6)$$

This quantity, which plays a central role in RMT (Bai & Silverstein, 2010), will be used in two primary ways. First, the normalized trace $\frac{1}{n} \text{tr} \mathbf{Q}(z)$ is the so-called *Stieltjes transform* of the eigenvalue distribution of \mathbf{K} , from which the eigenvalue distribution can be recovered, and the large n, p eigenvalue distribution of \mathbf{K} will be used to characterize the phase transition beyond which spectral clustering becomes theoretically possible (Corollary 2). Second, for $(\hat{\lambda}, \hat{\mathbf{v}})$, an eigenvalue-eigenvector pair of \mathbf{K} , and $\mathbf{a} \in \mathbb{R}^n$, a deterministic vector, by Cauchy’s integral formula, the “angle” between $\hat{\mathbf{v}}$ and \mathbf{a} is given by $|\hat{\mathbf{v}}^\top \mathbf{a}|^2 = -\frac{1}{2\pi i} \oint_{\Gamma(\hat{\lambda})} \mathbf{a}^\top \mathbf{Q}(z) \mathbf{a} dz$, where $\Gamma(\hat{\lambda})$ is a positively oriented contour surrounding $\hat{\lambda}$ only. Letting $\mathbf{a} = \mathbf{v}$, this will be exploited to characterize the spectral clustering error rate (Proposition 1).

From a technical perspective, unlike linear random matrix models, \mathbf{K} (and thus $\mathbf{Q}(z)$) involves nonlinear dependence between its entries. To break this difficulty, following the ideas of (Cheng & Singer, 2013), we exploit the fact that, by the central limit theorem, $\mathbf{z}_i^\top \mathbf{z}_j / \sqrt{p} \rightarrow \mathcal{N}(0, 1)$ in distribution as $p \rightarrow \infty$. As such, up to $\boldsymbol{\mu} \mathbf{v}^\top$, which is treated separately with a perturbation argument, the $[\mathbf{K}]_{ij}$ s asymptotically behave like a family of *dependent* standard Gaussian variables to which f is applied. Expanding f in a series of *orthogonal polynomials* with respect to the Gaussian measure allows for “unwrapping” this dependence. A few words on the theory of orthogonal polynomials (Abramowitz & Stegun, 1965; Andrews et al., 2000) are thus convenient to pursue our analysis.

Orthogonal polynomial framework. For a probability measure μ , let $\{P_l(x), l \geq 0\}$ be the orthonormal polynomials with respect to $\langle f, g \rangle \equiv \int f g d\mu$ obtained by the Gram-Schmidt procedure on the monomials $\{1, x, x^2, \dots\}$, such that $P_0(x) = 1$, P_l is of degree l and $\langle P_{l_1}, P_{l_2} \rangle = \delta_{l_1 - l_2}$. By the Riesz-Fischer theorem (Rudin, 1964, Theorem 11.43), for any function $f \in L^2(\mu)$, the set of square-integrable functions with respect to $\langle \cdot, \cdot \rangle$, one can formally expand f as

$$f(x) \sim \sum_{l=0}^{\infty} a_l P_l(x), \quad a_l = \int f(x) P_l(x) \mu(dx) \quad (7)$$

where “ $f \sim \sum_{l=0}^{\infty} a_l P_l$ ” indicates that $\|f - \sum_{l=0}^L a_l P_l\| \rightarrow 0$ as $L \rightarrow \infty$ with $\|f\|^2 = \langle f, f \rangle$.

To investigate the asymptotic behavior of \mathbf{K} , as $n, p \rightarrow \infty$, we make the following assumption on f .

Assumption 1. Let $\xi_p = \mathbf{z}_i^\top \mathbf{z}_j / \sqrt{p}$ and $\{P_{l,p}(x), l \geq 0\}$ be the orthonormal polynomials with respect to the measure μ_p of ξ_p . For $f \in L^2(\mu_p)$, $f(x) \sim \sum_{l=0}^{\infty} a_{l,p} P_{l,p}(x)$ with $a_{l,p}$ in (7) such that

1. $\sum_{l=0}^{\infty} a_{l,p} P_{l,p}(x) \mu_p(dx)$ converges in $L^2(\mu_p)$ to $f(x)$ uniformly over large p ; and
2. as $p \rightarrow \infty$, $\sum_{l=1}^{\infty} a_{l,p}^2 \rightarrow \nu \geq 0$ and, for $l = 0, 1, 2$, $a_{l,p} \rightarrow a_l$ converges with $a_0 = 0$.

Since $\xi_p \rightarrow \mathcal{N}(0, 1)$, the parameters a_0, a_1, a_2 and ν are simply moments of the standard Gaussian measure involving f . More precisely, for $\xi \sim \mathcal{N}(0, 1)$,

$$a_0 = \mathbb{E}[f(\xi)], \quad a_1 = \mathbb{E}[\xi f(\xi)], \quad \sqrt{2}a_2 = \mathbb{E}[\xi^2 f(\xi)] - a_0, \quad \nu = \mathbb{E}[f^2(\xi) - a_0^2] \geq a_1^2 + a_2^2. \quad (8)$$

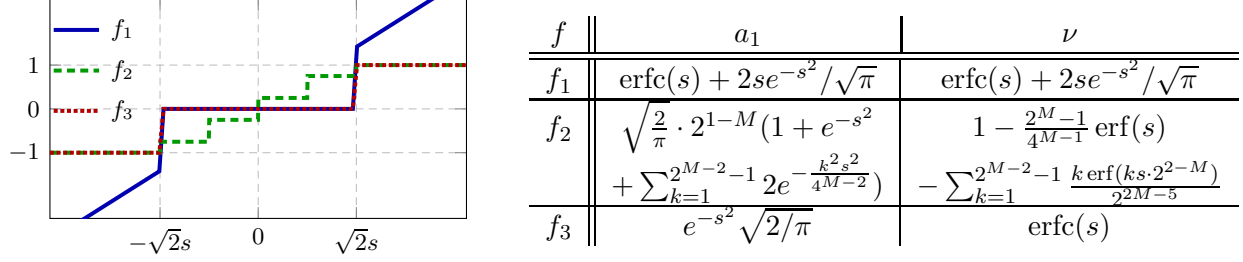


Figure 1: Visual representations of different functions f defined in (3)-(5) (**left**) and their associated parameters a_1 and ν (**right**) ($a_2 = 0$ for each of these f s) defined in Assumption 1.

Imposing the condition $a_0 = 0$ simply discards the *non-informative* rank-one matrix $a_0 \mathbf{1}_n \mathbf{1}_n^\top / \sqrt{p}$ from \mathbf{K} . The three parameters (a_1, a_2, ν) are of crucial significance in determining the spectral behavior of \mathbf{K} (see Theorem 1 below). The sparse f_1 , quantized f_2 , and binary f_3 of our primary interest all satisfy Assumption 1, with the corresponding $a_2 = 0$ (as we shall see in Corollary 1 below, this is important for the spectral clustering use case) and a_1, ν given in Figure 1-(right). With those introductory elements at hand, we are in position to present our main technical results.

3 Main Technical Results

Our main technical result, from which our performance-complexity trade-off analysis will follow, provides an asymptotic *deterministic equivalent* $\bar{\mathbf{Q}}(z)$ for the *random resolvent* \mathbf{Q} , defined in (6). (A deterministic equivalent is a deterministic matrix $\bar{\mathbf{Q}}(z)$ such that, for any deterministic sequence of matrices $\mathbf{A}_n \in \mathbb{R}^{n \times n}$ and vectors $\mathbf{a}_n, \mathbf{b}_n \in \mathbb{R}^n$ of bounded (spectral and Euclidean) norms, $\frac{1}{n} \operatorname{tr} \mathbf{A}_n (\mathbf{Q}(z) - \bar{\mathbf{Q}}(z)) \rightarrow 0$ and $\mathbf{a}_n^\top (\mathbf{Q}(z) - \bar{\mathbf{Q}}(z)) \mathbf{b}_n \rightarrow 0$ almost surely as $n, p \rightarrow \infty$. We denote this relation $\mathbf{Q}(z) \leftrightarrow \bar{\mathbf{Q}}(z)$.) This is given in the following theorem. The proof is in Appendix A.1.

Theorem 1 (Deterministic equivalent). *Let $n, p \rightarrow \infty$ with $p/n \rightarrow c \in (0, \infty)$, let $\mathbf{Q}(z)$ be defined in (6), and let $\Im[\cdot]$ denote the imaginary part of a complex number. Then, under Assumption 1,*

$$\mathbf{Q}(z) \leftrightarrow \bar{\mathbf{Q}}(z) = m(z) \mathbf{I}_n - \mathbf{V} \mathbf{\Lambda}(z) \mathbf{V}^\top, \quad \mathbf{\Lambda}(z) = \begin{bmatrix} \Theta(z) m^2(z) & \Theta(z) \Omega(z) \frac{\mathbf{v}^\top \mathbf{1}_n}{n} m(z) \\ \Theta(z) \Omega(z) \frac{\mathbf{v}^\top \mathbf{1}_n}{n} m(z) & \Theta(z) \Omega^2(z) \frac{(\mathbf{v}^\top \mathbf{1}_n)^2}{n^2} - \Omega(z) \end{bmatrix},$$

with $\sqrt{n} \mathbf{V} = [\mathbf{v}, \mathbf{1}_n]$, $\Omega(z) = \frac{a_2^2 (\kappa - 1) m^3(z)}{2c^2 - a_2^2 (\kappa - 1) m^2(z)}$, $\Theta(z) = \frac{a_1 \|\boldsymbol{\mu}\|^2}{c + a_1 m(z) (1 + \|\boldsymbol{\mu}\|^2) + a_1 \|\boldsymbol{\mu}\|^2 \Omega(z) (\mathbf{v}^\top \mathbf{1}_n)^2 / n^2}$, for κ the kurtosis of the entries of \mathbf{Z} , and $m(z)$ the unique solution, such that $\Im[m(z)] \cdot \Im[z] \geq 0$, to

$$-\frac{1}{m(z)} = z + \frac{a_1^2 m(z)}{c + a_1 m(z)} + \frac{\nu - a_1^2}{c} m(z). \quad (9)$$

As a consequence of Theorem 1, the *empirical spectral measure* $\omega_n = \frac{1}{n} \sum_{i=1}^n \delta_{\lambda_i(\mathbf{K})}$ of \mathbf{K} has a deterministic limit ω as $n, p \rightarrow \infty$, uniquely defined through its Stieltjes transform $m(z) \equiv \int (t - z)^{-1} \omega(dt)$ as the solution to (9).³ This limiting measure ω does *not* depend on the law of the independent entries of \mathbf{Z} , so long that they are sub-exponential, with zero mean and unit variance. In particular, taking $a_1 = 0$ in (9) gives the (rescaled) Wigner semi-circle law ω (Wigner, 1955), and taking $\nu = a_1^2$ (i.e., $a_l = 0$ for $l \geq 2$) gives the Marcenko-Pastur law ω (Marcenko & Pastur, 1967). See Remark 2 in Appendix A.2 for more discussions on this point.

³For $m(z)$ the Stieltjes transform of a measure ω , ω can be obtained via $\omega([a, b]) = \lim_{\epsilon \downarrow 0} \frac{1}{\pi} \int_a^b \Im[m(x + i\epsilon)] dx$ for all $a < b$ continuity points of ω .

Spurious non-informative spikes. Going beyond just the limiting spectral measure of \mathbf{K} , Theorem 1 also shows that *isolated eigenvalues* (often referred to as *spikes*) may be found in the eigenspectrum of \mathbf{K} at very specific locations. Such spikes and their associated eigenvectors are typically thought to provide information on the data class-structure (and they do when f is linear). However, when f is nonlinear, this is not always the case: it is possible that *not all* these spikes are “useful” in the sense of being informative about the class structure. This is made precise in the following, where we assume $\boldsymbol{\mu} = \mathbf{0}$, i.e., that there is no class structure. The proof is in Appendix A.2.

Corollary 1 (Non-informative spikes). *Assume $\boldsymbol{\mu} = \mathbf{0}$, $\kappa \neq 1$ and $a_2 \neq 0$, so that in the notations of Theorem 1, $\Theta(z) = 0$ and $\bar{\mathbf{Q}}(z) = m(z) + \Omega(z)\frac{1}{n}\mathbf{1}_n\mathbf{1}_n^\top$ for $\Omega(z)$ defined in Theorem 1. Then, if $x_\pm \equiv \pm\frac{1}{a_2}\sqrt{\frac{2}{\kappa-1}}$ satisfies $a_1x_\pm \neq \pm 1$ and $(\nu - a_1^2)x_\pm^2 + \frac{a_1^2x_\pm^2}{(1+a_1x_\pm)^2} < 1/c$, two eigenvalues of \mathbf{K} converge to $z_\pm = -\frac{1}{cx_\pm} - \frac{a_1^2x_\pm}{1+a_1x_\pm} - (\nu - a_1^2)x_\pm$ away from the support of ω . If instead $x_\pm = \pm 1/a_1$ for $a_1 \neq 0$, then a single eigenvalue of \mathbf{K} isolates with limit $z = -\frac{\nu}{a_1} - \frac{a_1(2-c)}{2c}$.*

Corollary 1 (combined with Theorem 1) says that, while the limiting spectrum ω is *universal* with respect to the distribution of the entries of \mathbf{Z} , the existence and position of the spurious non-informative spikes are *not universal* and depend on the kurtosis κ of the distribution. (See Figure 12 in Appendix A.2 for an example.) This is far from a mathematical curiosity. Given how nonlinear transformations are used in machine learning practice, being aware of the existence of *spurious non-informative spikes* in the eigenspectrum of \mathbf{K} (well separated from the bulk of eigenvalues, but that correspond to random noise instead of signal), as a function of properties of the nonlinear f , is of fundamental importance for downstream tasks. For example, for spectral clustering, their associated eigenvectors may be mistaken as informative ones by spectral clustering algorithms, even in the complete absence of classes. This is confirmed by Figure 2 where two isolated eigenvalues (on the right side of the bulk) are observed, with only the second largest one corresponds to an eigenvector that contains class-label information. For further discussions on this point, see Appendix A.2 and A.3.

Informative spikes. From Theorem 1, we see that the eigenspectrum of \mathbf{K} depends on f only via a_1 , a_2 , and ν . In particular, a_1 and ν determine the limiting spectral measure ω . From Corollary 1, we see that a_2 contributes by (i) introducing (at most two) non-informative spikes and (ii) reducing the ratio a_1/ν (since $\nu = \sum_{i \geq 1} a_i^2$), thereby necessarily *enlarging* the support of ω (see Remark 2 in Appendix A.2). Taking $a_2 = 0$ reduces the length of the support of ω and, as such, maximizes the “chance” of the appearance of an informative spike (the eigenvector of which is positively correlated with the label vector \mathbf{v}). See Remark 1 below for a more precise statement.

In particular, by taking $a_2 = 0$ and $a_1 \neq 0$, we obtain only informative spikes, and we can characterize a phase transition depending on the SNR ρ . The proof of the following is in Appendix A.3.

Corollary 2 (Informative spike and a phase transition). *For $a_1 > 0$ and $a_2 = 0$, let*

$$F(x) = x^4 + 2x^3 + \left(1 - \frac{c\nu}{a_1^2}\right)x^2 - 2cx - c, \quad G(x) = \frac{a_1}{c}(1+x) + \frac{a_1}{x} + \frac{\nu - a_1^2}{a_1} \frac{1}{1+x}, \quad (10)$$

and let γ be the largest real solution to $F(\gamma) = 0$. Then, under Assumption 1, we have $\sqrt{c} \leq \gamma \leq \sqrt{c\nu}/a_1$, and the largest eigenpair $(\hat{\lambda}, \hat{\mathbf{v}})$ of \mathbf{K} satisfies

$$\hat{\lambda} \rightarrow \lambda = \begin{cases} G(\rho) & \rho > \gamma, \\ G(\gamma) & \rho \leq \gamma; \end{cases} \quad \frac{|\hat{\mathbf{v}}^\top \mathbf{v}|^2}{n} \rightarrow \alpha = \begin{cases} \frac{F(\rho)}{\rho(1+\rho)^3} & \rho > \gamma, \\ 0 & \rho \leq \gamma; \end{cases} \quad (11)$$

almost surely as $n, p \rightarrow \infty$, $p/n \rightarrow c \in (0, \infty)$, where we recall $\rho \equiv \lim_{p \rightarrow \infty} \|\boldsymbol{\mu}\|^2$ and $\|\mathbf{v}\| = \sqrt{n}$.

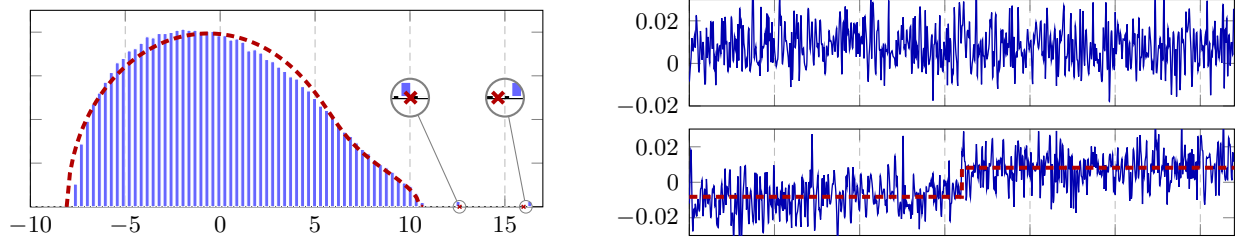


Figure 2: **(Left)** Histogram of eigenvalues of \mathbf{K} (blue) versus the limiting spectrum and spikes (red). **(Right)** Eigenvectors of the largest (top) and second largest (bottom) eigenvalues of \mathbf{K} (blue), versus the rescaled class label $\alpha \mathbf{v} / \sqrt{n}$ (red, from Corollary 2). $f(t) = \sin(t) - 3 \cos(t) + 3/\sqrt{e}$, $p = 800$, $n = 6400$, $\boldsymbol{\mu} = 1.1 \cdot \mathbf{1}_p / \sqrt{p}$, $\mathbf{v} = [-\mathbf{1}_{n/2}; \mathbf{1}_{n/2}]$ on Student-t data with $\kappa = 5$.

Here the statement on the eigenvector alignment α is in line with (Cheng, 2013, Conjecture 4.4).

Without loss of generality, we discuss only the case $a_1 > 0$.⁴ For $a_1 > 0$, both $F(x)$ and $G(x)$ are increasing functions on $x \in (\gamma, \infty)$. Then, as expected, both λ and α increase with the SNR ρ . Moreover, the phase transition point γ is an increasing function of c and of ν/a_1^2 . As such, the optimal choice of f in the sense of the smallest phase transition point is the linear function $f(t) = t$ with $a_1 = \nu = 1$ and $\gamma = \sqrt{c}$. This recovers the classical random matrix result (Baik et al., 2005).

4 Clustering performance of sparse and quantized operators

We start, in Section 4.1, by providing a sharp asymptotic characterization of the clustering error rate and demonstrating the optimality of the linear function under (1). Then, in Section 4.2, we discuss the advantageous performance of the proposed selective sparsification approach (with f_1) versus the uniform or subsampling approach studied previously (Zarrouk et al., 2020). Finally, in Section 4.3, we derive the optimal truncation threshold s_{opt} , for both quantized f_2 and binary f_3 , so as to achieve an optimal performance-complexity trade-off for a given storage budget.

4.1 Performance of spectral clustering

The technical results in Section 3 provide conditions under which \mathbf{K} admits an informative eigenvector $\hat{\mathbf{v}}$ that is non-trivially correlated with the class label vector \mathbf{v} (and thus that is exploitable for spectral clustering) in the $n, p \rightarrow \infty$ limit. Since the exact (limiting) alignment $|\mathbf{v}^\top \hat{\mathbf{v}}|$ is known, along with an additional argument on the normal fluctuations of $\hat{\mathbf{v}}$, we have the following result for the performance of the spectral clustering method. The proof is in Appendix A.4.

Proposition 1 (Performance of spectral clustering). *Let Assumption 1 hold, let $a_1 > 0, a_2 = 0$, and let $\hat{C}_i = \text{sign}([\hat{\mathbf{v}}]_i)$ be the estimate of the underlying class C_i of the datum \mathbf{x}_i , with the convention $\hat{\mathbf{v}}^\top \mathbf{v} \geq 0$, for $\hat{\mathbf{v}}$ the top eigenvector of \mathbf{K} . Then, the misclassification rate satisfies $\frac{1}{n} \sum_{i=1}^n \delta_{\hat{C}_i \neq C_i} \rightarrow \frac{1}{2} \text{erfc}(\sqrt{\alpha/(2-2\alpha)})$, almost surely, as $n, p \rightarrow \infty$, for $\alpha \in [0, 1)$ defined in (11).*

Despite being asymptotic results valid in the $n, p \rightarrow \infty$ limit, the results of Proposition 1 and Corollary 2 closely match empirical results for n, p in the hundreds. This is illustrated in Figure 3. Proposition 1 further confirms that the misclassification rate, being a decreasing function of α , increases with ν/a_1^2 (for c and ρ fixed). This leads to the following remark.

⁴Otherwise we could consider $-\mathbf{K}$ instead of \mathbf{K} and the largest eigenvalue becomes the smallest one.

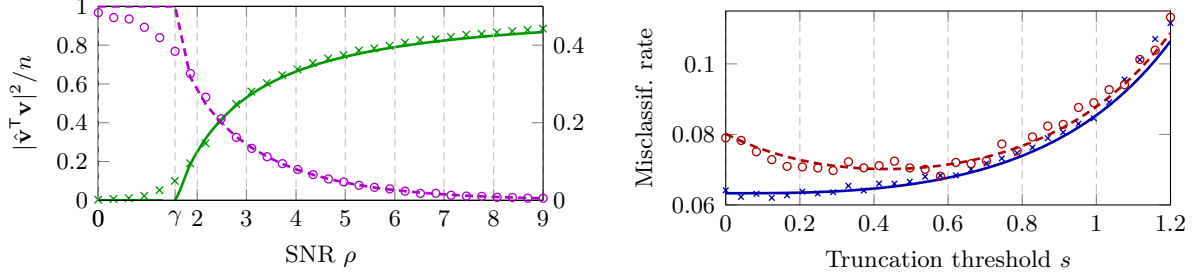


Figure 3: **(Left)** Empirical alignment $|\hat{\mathbf{v}}^T \mathbf{v}|^2/n$ (green crosses) and misclassification rate (purple circles) in markers versus their limiting behaviors in lines, for $f(t) = \text{sign}(t)$, as a function of SNR ρ . **(Right)** Misclassification rate as a function of the truncation thresholds s of sparse f_1 (blue crosses) and binary f_3 (red circles) with $\rho = 4$. Here, $p = 512$, $n = 256$, $\boldsymbol{\mu} \propto \mathcal{N}(\mathbf{0}, \mathbf{I}_p)$, $\mathbf{v} = [-\mathbf{1}_{n/2}; \mathbf{1}_{n/2}]$ on Gaussian data, and we averaged over 250 runs.

Remark 1 (Optimality of linear function). *Since both the phase transition point γ and the misclassification rate grow with ν/a_1^2 , the linear function $f(t) = t$ with the minimal $\nu/a_1^2 = 1$ is optimal in the sense of (i) achieving the smallest SNR ρ or the largest ratio $c = \lim p/n$ (i.e., the fewest samples n) necessary to observe an informative (isolated) eigenvector, and (ii) upon existence of such an isolated eigenvector, reaching the lowest classification error rate.*

According to Remark 1, any f with $\nu/a_1^2 > 1$ induces performance degeneration (compared to the optimal linear function). However, by choosing f to be one of the functions f_1, f_2, f_3 defined in (3)-(5), one may trade clustering performance optimality for reduced storage size and computational time. Figure 4 displays the decay in clustering performance and the gain in storage size of the sparse f_1 , quantized f_2 , and binary f_3 , when compared to the optimal but “dense” linear function. As $s \rightarrow 0$, both performance and storage size under f_1 naturally approach those of the linear function. This is unlike f_2 or f_3 , which approach the sign function. For $s \gg 1$, the performance under sparse f_1 becomes comparable to that of binary f_3 (which is significantly worse than quantized but non-sparse f_2) but for a larger storage cost. In particular, using f_2 or f_3 in the setting of Figure 4, one can reduce the storage size by a factor of 32 or 64 (IEEE standard single- or double-precision floating-point format), at the price of a performance drop less than 1%.

4.2 Comparison to uniform sparsification and subsampling

From Figure 4, we see that the classification error and storage gain of the sparse f_1 increase monotonically, as the truncation threshold s grows. For f_1 , the number of non-zero entries of \mathbf{K} is approximately $\text{erfc}(s)n^2$ with truncation threshold s . Thus, the *sparsity level*

$$\varepsilon_{\text{selec}} = \text{erfc}(s) \in [0, 1] \quad (12)$$

can be defined and compared to uniform sparsification or subsampling approaches.

Recall (from the introduction) that the cost of spectral clustering may be reduced by subsampling the whole dataset in $1/\varepsilon_{\text{sub}}$ chunks of $n\varepsilon_{\text{sub}}$ data vectors each. Alternatively, as investigated recently (Zarrouk et al., 2020), the cost can be reduced by uniformly zeroing-out $\mathbf{X}^T \mathbf{X}$ with a symmetric mask matrix \mathbf{B} , with $\mathbf{B}_{ij} \sim \text{Bern}(\varepsilon_{\text{unif}})$ for $1 \leq i < j \leq n$ and $\mathbf{B}_{ii} = 0$. On average, a proportion $1 - \varepsilon_{\text{unif}}$ of the entries of $\mathbf{X}^T \mathbf{X}$ is set to zero, so that $\varepsilon_{\text{unif}} \in [0, 1]$ controls the sparsity level (and thus the storage size as well as computational time). Similar to our Corollary 2, the associated eigenvector alignment (and thus the clustering accuracy via Proposition 1) in both cases can be

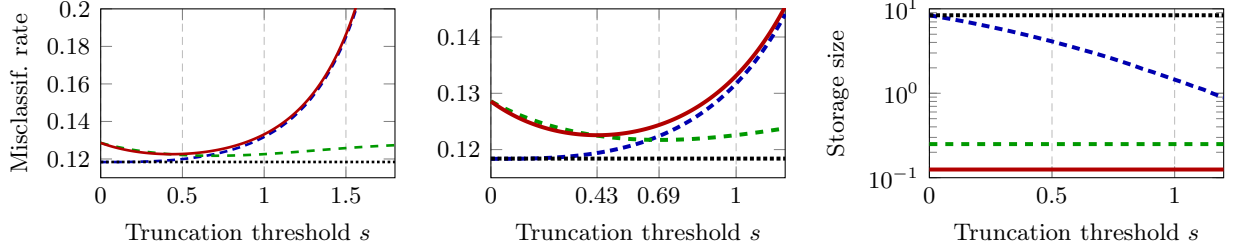


Figure 4: Clustering performance (**left**, a zoom-in in **middle**) and storage size (MB) (**right**) of f_1 (**blue**), f_2 with $M = 2$ (**green**), f_3 (**red**), and linear $f(t) = t$ (**black**), versus the truncation threshold s , for SNR $\rho = 2$, $c = 1/2$ and $n = 10^3$, with 64 bits per entry for non-quantized matrices.

derived. Specifically, taking $\varepsilon_{\text{unif}} = a_1^2/\nu$ in (Zarrouk et al., 2020, Theorem 3.2), we obtain the same $F(x)$ as in our Corollary 2 and therefore the same phase transition point γ and eigenvector alignment α . As for subsampling, its performance can be obtained by letting $a_1^2 = \nu$ and changing c into $c/\varepsilon_{\text{sub}}$ in the formulas of $F(x)$ and $G(x)$ of our Corollary 2. Consequently, the same clustering performance is achieved by either uniform or selective sparsification (with f_1) with

$$\varepsilon_{\text{unif}} = a_1^2/\nu = \text{erfc}(s) + 2se^{-s^2}/\sqrt{\pi} > \text{erfc}(s) = \varepsilon_{\text{selec}}, \quad (13)$$

and our proposed selective sparsification approach thus leads to *strictly sparser* matrices. Moreover, their ratio

$$r(s) = \text{erfc}(s)/(\text{erfc}(s) + 2se^{-s^2}/\sqrt{\pi}) \quad (14)$$

is a decreasing function of s and approximates as $r(s) \sim (1 + s^2)^{-1}/2$ for $s \gg 1$,⁵ meaning that the gain in storage size and computational time is more significant as the matrix becomes sparser. This is depicted in Figure 5-(left).

Fixing α in Corollary 2 to achieve a given clustering performance level (via Proposition 1), one may then retrieve “equi-performance” curves in the (ε, ρ) -plane, for uniform sparsification, selective sparsification, and subsampling. This is displayed in Figure 5-(right), showing that a dramatic performance gain is achieved by the proposed selective sparsification. Besides, here for $c = 2$, as much as 80% sparsity may be obtained with selective sparsification at constant SNR ρ , with virtually no performance loss (red curves are almost flat on $\varepsilon \in [0.2, 1]$). This fails to hold for uniform sparsification (Zarrouk et al. (2020) obtain such a result only when $c \lesssim 0.1$) or subsampling.

4.3 Optimally quantized and binarized matrices

From Figure 4, we see that the classification error of the quantized $f_2(M; s; t)$ and binarized $f_3(s; t)$ do *not* increase monotonically with the truncation threshold s . It can be shown (and visually confirmed in Figure 4) that, for a given $M \geq 2$, the ratio ν/a_1^2 of both f_2 and f_3 is convex in s and has a unique minimum. This leads to the following optimal design result for f_2 and f_3 , respectively, the proof of which is straightforward.

Proposition 2 (Optimal design of quantized and binarized functions). *Under the assumptions and notations of Proposition 1, the classification error rate is minimized at $s = s_{\text{opt}}$ with*

1. s_{opt} the unique solution to $a_1(s_{\text{opt}})\nu'(s_{\text{opt}}) = 2a_1'(s_{\text{opt}})\nu(s_{\text{opt}})$ for quantized f_2 , with $a_1'(s)$ and $\nu'(s)$ the corresponding derivatives with respect to s in Figure 1-(right); and

⁵We use here the asymptotic expansion $\text{erfc}(s) = \frac{e^{-s^2}}{s\sqrt{\pi}} \left[1 + \sum_{k=1}^{\infty} (-1)^k \cdot \frac{1 \cdot 3 \cdots (2k-1)}{(2s^2)^k} \right]$.

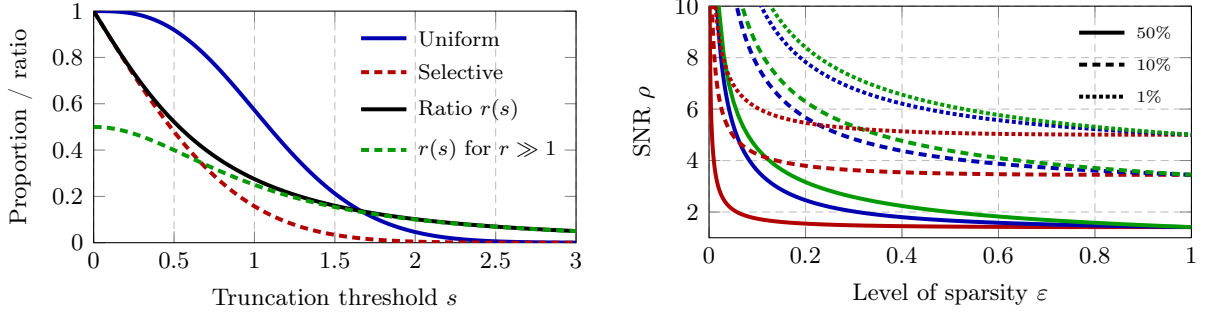


Figure 5: **(Left)** Proportion of non-zero entries with uniform versus selective sparsification f_1 and their ratio, as a function of the truncation threshold s . **(Right)** Comparison of 1%, 10% classification error and phase transition (i.e., 50% error) curves between subsampling (green), uniform (blue) and selective sparsification f_1 (red), as a function of sparsity level ε and SNR ρ , for $c = 2$.

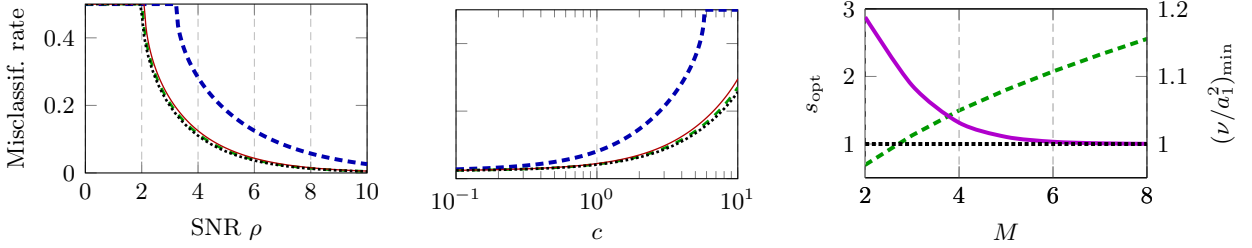


Figure 6: Performance of f_1 (blue), f_2 with $M = 3$ (green) and f_3 (red) of the same storage size, versus SNR for $c = 4$ (left) and versus c for SNR $\rho = 4$ (middle). (Right) Optimal threshold s_{opt} (green) and $(\nu/a_1^2)_{\text{min}}$ (purple) of f_2 versus M . Curves for linear $f(t) = t$ are displayed in black.

2. $s_{\text{opt}} = \exp(-s_{\text{opt}}^2)/(2\sqrt{\pi} \text{erfc}(s_{\text{opt}})) \approx 0.43$ for binary f_3 , with $\nu/a_1^2 \approx 1.24$ and level of sparsity $\varepsilon \approx 0.54$.

Therefore, the optimal threshold s_{opt} for quantized f_2 or binary f_3 under (1) is *problem-independent*, as it depends neither on ρ nor on c . In particular, note that (i) the binary $f_3(s_{\text{opt}}; \cdot)$ is *consistently* better than $f(t) = \text{sign}(t)$ for which $\nu/a_1^2 = \pi/2 \approx 1.57 > 1.24$; and (ii) the performance of quantized f_2 can be *worse*, though very slightly, than that of binary f_3 for small s , but significantly better for not-too-small s . These are visually confirmed in the left and middle displays of Figure 4.

As already observed in Figure 4-(right), a significant gain in storage size can be achieved by using f_2 or f_3 , versus the performance-optimal but dense linear function, with virtually no performance loss. Figure 6 compares the performance of the optimally designed f_2 and f_3 , to sparse f_1 that has *approximately* the same storage size.⁶ A significant drop in classification error is observed by using quantization f_2 or binarization f_3 rather than sparsification f_1 . Also, the performances of f_2 and f_3 are extremely close to the theoretical optimal (met by $f(t) = t$). This is further confirmed by Figure 6-(right) where, for the optimal f_2 , the ratio ν/a_1^2 gets close to 1, for all $M \geq 5$.

Figure 7 next evaluates the clustering performance, the proportion of nonzero entries in \mathbf{K} , and the computational time of the top eigenvector, for sparse f_1 and binary f_3 , versus linear $f(t) = t$, as a function of the truncation threshold s , on the popular MNIST datasets (LeCun et al., 1998).

⁶We set the truncation threshold s of f_1 such that $\text{erfc}(s) = 3/64$, so that the storage size of the sparse f_1 (64 bits per non-zero entry) is the same as the quantized f_2 with $M = 3$ (with 3 bits per non-zero entry), which is *three times* that of the binary f_3 .

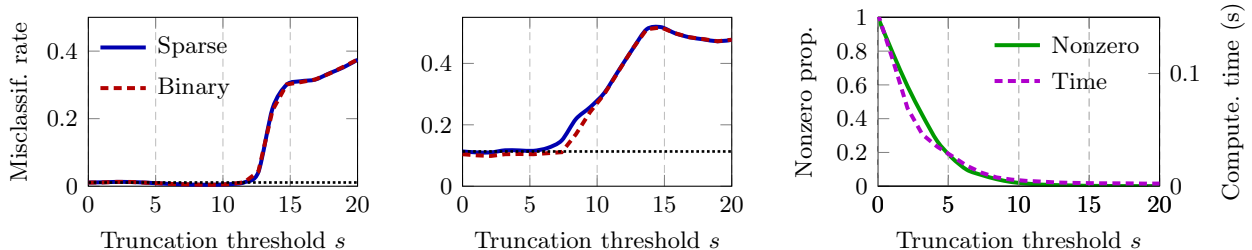


Figure 7: Clustering performance of sparse f_1 and binary f_3 (**left** and **middle**), proportion of nonzero entries and computational time of the top eigenvector for f_3 (**right**), as a function of the truncation threshold s on the MNIST dataset: digits (0, 1) (**left**) and (5, 6) (**middle** and **right**) with $n = 2048$ and performance of the linear function in **black**. Results averaged over 100 runs.

Depending on (the SNR ρ of) the task, up to 90% of the entries can be discarded almost “for free”. Moreover, the curves of the binary f_3 appear strikingly close to those of the sparse f_1 , showing the additional advantage of using the former to further reduce the storage size of \mathbf{K} . More empirical results on various datasets are provided in Appendix B to confirm our observations in Figure 7.

5 Concluding remarks

We have evaluated **performance-complexity trade-offs** when sparsifying, quantizing, and binarizing a linear kernel matrix via a thresholding operator. Our main technical result **characterizes the change in the eigenspectrum under these operations**; and we have shown that, **under an information-plus-noise mixture data, sparsification and quantization, when carefully employed, maintain the informative eigenstructure and incur almost negligible performance loss in spectral clustering**. Empirical results on real data demonstrate that these conclusions hold far beyond the present statistical model.

Our results open the door to theoretical investigation of a broad range of cost-efficient linear algebra methods in machine learning, including subsampling techniques (Mensch et al., 2017; Roosta-Khorasani & Mahoney, 2019), distributed optimization (Wang et al., 2018), randomized linear algebra algorithms (Mahoney, 2011; Drineas & Mahoney, 2016), and quantization for improved training and/or inference (Dong et al., 2019; Shen et al., 2020). Also, given recent interest in viewing neural networks from the perspective of RMT (Martin & Mahoney, 2018; Li & Nguyen, 2018; Seddik et al., 2018; Jacot et al., 2019; Liu & Dobriban, 2019; Martin & Mahoney, 2019, 2020a,b), our results open the door to understanding and improving performance-complexity trade-offs far beyond kernel methods, e.g., to sparse, quantized, or even binary neural networks (Courbariaux et al., 2016; Lin et al., 2017) that go beyond kernel methods (Rahimi & Recht, 2008; Jacot et al., 2018).

Acknowledgments

We would like to acknowledge DARPA, NSF, and ONR for providing partial support of this work. Couillet’s work is partially supported by MIAI at University Grenoble-Alpes (ANR-19-P3IA-0003).

References

Milton Abramowitz and Irene A Stegun. *Handbook of mathematical functions: with formulas, graphs, and mathematical tables*, volume 55. Courier Corporation, 1965.

- Dimitris Achlioptas and Frank McSherry. Fast computation of low-rank matrix approximations. *Journal of the ACM (JACM)*, 54(2):9-es, 2007.
- George E Andrews, Richard Askey, and Ranjan Roy. *Special functions*, volume 71. Cambridge university press, 2000.
- Zhidong Bai and Jack W Silverstein. *Spectral analysis of large dimensional random matrices*, volume 20. Springer, 2010.
- Jinho Baik, Gérard Ben Arous, and Sandrine Péché. Phase transition of the largest eigenvalue for nonnull complex sample covariance matrices. *The Annals of Probability*, 33(5):1643–1697, 2005.
- Xiuyuan Cheng. *Random matrices in high-dimensional data analysis*. PhD thesis, Princeton, NJ: Princeton University, 2013. URL <http://arks.princeton.edu/ark:/88435/dsp01wh246s26t>.
- Xiuyuan Cheng and Amit Singer. The spectrum of random inner-product kernel matrices. *Random Matrices: Theory and Applications*, 2(04):1350010, 2013.
- Tarin Clanuwat, Mikel Bober-Irizar, Asanobu Kitamoto, Alex Lamb, Kazuaki Yamamoto, and David Ha. Deep learning for classical japanese literature, 2018.
- Matthieu Courbariaux, Itay Hubara, Daniel Soudry, Ran El-Yaniv, and Yoshua Bengio. Binarized neural networks: Training deep neural networks with weights and activations constrained to +1 or −1. *arXiv preprint arXiv:1602.02830*, 2016.
- Jia Deng, Wei Dong, Richard Socher, Li-Jia Li, Kai Li, and Li Fei-Fei. ImageNet: A large-scale hierarchical image database. In *2009 IEEE conference on computer vision and pattern recognition*, pp. 248–255. Ieee, 2009.
- Yen Do and Van Vu. The spectrum of random kernel matrices: universality results for rough and varying kernels. *Random Matrices: Theory and Applications*, 2(03):1350005, 2013.
- Zhen Dong, Zhewei Yao, Amir Gholami, Michael W Mahoney, and Kurt Keutzer. HAWQ: Hessian aware quantization of neural networks with mixed-precision. In *Proceedings of the IEEE International Conference on Computer Vision*, pp. 293–302, 2019.
- Petros Drineas and Michael W Mahoney. RandNLA: randomized numerical linear algebra. *Communications of the ACM*, 59(6):80–90, 2016.
- Petros Drineas and Anastasios Zouzias. A note on element-wise matrix sparsification via a matrix-valued Bernstein inequality. *Information Processing Letters*, 111(8):385–389, 2011.
- Noureddine El Karoui. On information plus noise kernel random matrices. *The Annals of Statistics*, 38(5):3191–3216, 2010.
- Zhou Fan and Andrea Montanari. The spectral norm of random inner-product kernel matrices. *Probability Theory and Related Fields*, 173(1-2):27–85, 2019.
- Gene H. Golub and Charles F. Van Loan. *Matrix Computations*. The Johns Hopkins University Press, third edition, 1996.
- Arthur Jacot, Franck Gabriel, and Clément Hongler. Neural Tangent Kernel: Convergence and generalization in neural networks. In *Advances in neural information processing systems*, pp. 8571–8580, 2018.

- Arthur Jacot, Franck Gabriel, and Clement Hongler. The asymptotic spectrum of the Hessian of DNN throughout training. In *International Conference on Learning Representations*, 2019.
- Arun Kadavankandy and Romain Couillet. Asymptotic gaussian fluctuations of spectral clustering eigenvectors. In *2019 IEEE 8th International Workshop on Computational Advances in Multi-Sensor Adaptive Processing (CAMSAP)*, pp. 694–698. IEEE, 2019.
- Yann LeCun, Léon Bottou, Yoshua Bengio, and Patrick Haffner. Gradient-based learning applied to document recognition. *Proceedings of the IEEE*, 86(11):2278–2324, 1998.
- Ping Li and Phan-Minh Nguyen. On random deep weight-tied autoencoders: Exact asymptotic analysis, phase transitions, and implications to training. In *International Conference on Learning Representations*, 2018.
- Zhenyu Liao and Romain Couillet. Inner-product kernels are asymptotically equivalent to binary discrete kernels. *arXiv preprint arXiv:1909.06788*, 2019.
- Xiaofan Lin, Cong Zhao, and Wei Pan. Towards accurate binary convolutional neural network. In *Advances in Neural Information Processing Systems*, pp. 345–353, 2017.
- Sifan Liu and Edgar Dobriban. Ridge Regression: Structure, Cross-Validation, and Sketching. In *International Conference on Learning Representations*, 2019.
- Anna Lytova and Leonid Pastur. Central limit theorem for linear eigenvalue statistics of random matrices with independent entries. *The Annals of Probability*, 37(5):1778–1840, 2009.
- Michael W Mahoney. Randomized Algorithms for Matrices and Data. *Foundations and Trends® in Machine Learning*, 3(2):123–224, 2011.
- Michael W Mahoney. Lecture notes on spectral graph methods. *arXiv preprint arXiv:1608.04845*, 2016.
- Vladimir A Marcenko and Leonid Andreevich Pastur. Distribution of eigenvalues for some sets of random matrices. *Mathematics of the USSR-Sbornik*, 1(4):457, 1967.
- Charles H Martin and Michael W Mahoney. Implicit self-regularization in deep neural networks: Evidence from random matrix theory and implications for learning. *arXiv preprint arXiv:1810.01075*, 2018.
- Charles H Martin and Michael W Mahoney. Traditional and heavy tailed self regularization in neural network models. In *International Conference on Machine Learning*, pp. 4284–4293, 2019.
- Charles H Martin and Michael W Mahoney. Heavy-tailed universality predicts trends in test accuracies for very large pre-trained deep neural networks. In *Proceedings of the 2020 SIAM International Conference on Data Mining*, pp. 505–513. SIAM, 2020a.
- Charles H Martin and Michael W Mahoney. Predicting trends in the quality of state-of-the-art neural networks without access to training or testing data. *arXiv preprint arXiv:2002.06716*, 2020b.
- Arthur Mensch, Julien Mairal, Bertrand Thirion, and Gaël Varoquaux. Stochastic subsampling for factorizing huge matrices. *IEEE Transactions on Signal Processing*, 66(1):113–128, 2017.
- Vinay Uday Prabhu. Kannada-MNIST: A new handwritten digits dataset for the Kannada language. *arXiv preprint arXiv:1908.01242*, 2019.

- Ali Rahimi and Benjamin Recht. Random features for large-scale kernel machines. In *Advances in neural information processing systems*, pp. 1177–1184, 2008.
- Farbod Roosta-Khorasani and Michael W Mahoney. Sub-sampled Newton methods. *Mathematical Programming*, 174(1-2):293–326, 2019.
- Walter Rudin. *Principles of mathematical analysis*, volume 3. McGraw-hill New York, 1964.
- Alaa Saade, Florent Krzakala, and Lenka Zdeborová. Spectral clustering of graphs with the Bethe Hessian. In *Advances in Neural Information Processing Systems*, pp. 406–414, 2014.
- Mohamed El Amine Seddik, Mohamed Tamaazousti, and Romain Couillet. A kernel random matrix-based approach for sparse PCA. In *International Conference on Learning Representations*, 2018.
- Mohamed El Amine Seddik, Cosme Louart, Mohamed Tamaazousti, and Romain Couillet. Random matrix theory proves that deep learning representations of GAN-data behave as gaussian mixtures. *arXiv preprint arXiv:2001.08370*, 2020.
- Sheng Shen, Zhen Dong, Jiayu Ye, Linjian Ma, Zhewei Yao, Amir Gholami, Michael W Mahoney, and Kurt Keutzer. Q-BERT: Hessian Based Ultra Low Precision Quantization of BERT. In *AAAI*, pp. 8815–8821, 2020.
- Jack W Silverstein and ZD Bai. On the empirical distribution of eigenvalues of a class of large dimensional random matrices. *Journal of Multivariate analysis*, 54(2):175–192, 1995.
- Jack W Silverstein and Sang-Il Choi. Analysis of the limiting spectral distribution of large dimensional random matrices. *Journal of Multivariate Analysis*, 54(2):295–309, 1995.
- Nitish Srivastava, Geoffrey Hinton, Alex Krizhevsky, Ilya Sutskever, and Ruslan Salakhutdinov. Dropout: a simple way to prevent neural networks from overfitting. *The journal of machine learning research*, 15(1):1929–1958, 2014.
- Christian Szegedy, Wei Liu, Yangqing Jia, Pierre Sermanet, Scott Reed, Dragomir Anguelov, Dumitru Erhan, Vincent Vanhoucke, and Andrew Rabinovich. Going deeper with convolutions. In *Proceedings of the IEEE conference on computer vision and pattern recognition*, pp. 1–9, 2015.
- Terence Tao, Van Vu, and Manjunath Krishnapur. Random matrices: Universality of ESDs and the circular law. *The Annals of Probability*, 38(5):2023–2065, 2010.
- Dan Voiculescu. Addition of certain non-commuting random variables. *Journal of functional analysis*, 66(3):323–346, 1986.
- Ulrike Von Luxburg. A tutorial on spectral clustering. *Statistics and computing*, 17(4):395–416, 2007.
- Shusen Wang, Fred Roosta, Peng Xu, and Michael W Mahoney. GIANT: Globally improved approximate Newton method for distributed optimization. In *Advances in Neural Information Processing Systems*, pp. 2332–2342, 2018.
- Eugene P. Wigner. Characteristic vectors of bordered matrices with infinite dimensions. *Annals of Mathematics*, 62(3):548–564, 1955.
- Han Xiao, Kashif Rasul, and Roland Vollgraf. Fashion-MNIST: a Novel Image Dataset for Benchmarking Machine Learning Algorithms, 2017.

A Proofs and related discussions

Under the mixture model (1), the data matrix $\mathbf{X} \in \mathbb{R}^{p \times n}$ can be compactly written as

$$\mathbf{X} = \mathbf{Z} + \boldsymbol{\mu} \mathbf{v}^\top, \quad (15)$$

for $\mathbf{Z} \in \mathbb{R}^{p \times n}$ having i.i.d. zero-mean, unit-variance, κ -kurtosis, sub-exponential entries and $\mathbf{v} \in \{\pm 1\}^n$ so that $\|\mathbf{v}\| = \sqrt{n}$. Recall also the following notations:

$$\mathbf{K} = \left\{ \delta_{i \neq j} f(\mathbf{x}_i^\top \mathbf{x}_j / \sqrt{p}) / \sqrt{p} \right\}_{i,j=1}^n, \quad \mathbf{Q}(z) \equiv (\mathbf{K} - z \mathbf{I}_n)^{-1}. \quad (16)$$

A.1 Proof of Theorem 1

The proof of Theorem 1 comes in the following two steps:

1. show that the random quantities $\frac{1}{n} \text{tr} \mathbf{A}_n \mathbf{Q}(z)$ and $\mathbf{a}_n^\top \mathbf{Q}(z) \mathbf{b}_n$ of interest concentrate around their expectations in the sense that

$$\frac{1}{n} \text{tr} \mathbf{A}_n (\mathbf{Q}(z) - \mathbb{E}[\mathbf{Q}(z)]) \rightarrow 0, \quad \mathbf{a}_n^\top (\mathbf{Q}(z) - \mathbb{E}[\mathbf{Q}(z)]) \mathbf{b}_n \rightarrow 0, \quad (17)$$

almost surely as $n, p \rightarrow \infty$; and

2. show that the sought-for *deterministic equivalent* $\bar{\mathbf{Q}}(z)$ given in Theorem 1 is an asymptotic approximation for the expectation of the resolvent $\mathbf{Q}(z)$ defined in (6) in the sense that

$$\|\mathbb{E}[\mathbf{Q}] - \bar{\mathbf{Q}}\| \rightarrow 0, \quad (18)$$

as $n, p \rightarrow \infty$.

The concentration of trace forms in the first item has been established in (Cheng & Singer, 2013; Do & Vu, 2013), and the bilinear forms follow similarly. Here we focus on the second item to show that $\|\mathbb{E}[\mathbf{Q}] - \bar{\mathbf{Q}}\| \rightarrow 0$ in the large n, p limit.

In the sequel, we use $o(1)$ and $o_{\|\cdot\|}(1)$ for scalars or matrices of (almost surely if being random) vanishing absolute values or operator norms as $n, p \rightarrow \infty$.

To establish $\|\mathbb{E}[\mathbf{Q}] - \bar{\mathbf{Q}}\| \rightarrow 0$, we need to show subsequently that:

1. under (15), the random matrix \mathbf{K} defined in (2) admits a spiked-model approximation, that is

$$\mathbf{K} = \tilde{\mathbf{K}}_0 + \mathbf{U} \boldsymbol{\Lambda} \mathbf{U}^\top + o_{\|\cdot\|}(1), \quad (19)$$

for some full rank random (noise) matrix $\tilde{\mathbf{K}}_0$ and low rank (information) matrix $\mathbf{U} \boldsymbol{\Lambda} \mathbf{U}^\top$ to be specified; and

2. the matrix inverse $(\tilde{\mathbf{K}}_0 - \mathbf{U} \boldsymbol{\Lambda} \mathbf{U}^\top - z \mathbf{I}_n)^{-1}$ can be decomposed with the Woodbury identity, so that

$$\mathbf{Q} = (\tilde{\mathbf{K}}_0 - \mathbf{U} \boldsymbol{\Lambda} \mathbf{U}^\top - z \mathbf{I}_n)^{-1} + o_{\|\cdot\|}(1) = \tilde{\mathbf{Q}}_0 - \tilde{\mathbf{Q}}_0 \mathbf{U} (\boldsymbol{\Lambda}^{-1} + \mathbf{U}^\top \tilde{\mathbf{Q}}_0 \mathbf{U})^{-1} \mathbf{U}^\top \tilde{\mathbf{Q}}_0 + o_{\|\cdot\|}(1), \quad (20)$$

with $\tilde{\mathbf{Q}}_0(z) \equiv (\tilde{\mathbf{K}}_0 - z \mathbf{I}_n)^{-1}$; and

3. the expectation of the right-hand side of (20) is close to $\bar{\mathbf{Q}}$ in the large n, p limit, allowing us to conclude the proof of Theorem 1.

To establish (19), we denote the “noise-only” null model with $\|\boldsymbol{\mu}\| = 0$ by writing $\mathbf{K} = \mathbf{K}_0$ such that

$$[\mathbf{K}_0]_{ij} = \delta_{i \neq j} f(\mathbf{z}_i^\top \mathbf{z}_j / \sqrt{p}) / \sqrt{p}. \quad (21)$$

With a combinatorial argument, it has been shown (Fan & Montanari, 2019) that

$$\left\| \mathbf{K}_0 - \tilde{\mathbf{K}}_0 - \frac{a_2}{\sqrt{2}p} (\boldsymbol{\psi} \mathbf{1}_n^\top + \mathbf{1}_n \boldsymbol{\psi}^\top) \right\| \rightarrow 0, \quad (22)$$

almost surely as $n, p \rightarrow \infty$, for $\tilde{\mathbf{K}}_0$ such that $(\tilde{\mathbf{K}}_0 - z \mathbf{I}_n)^{-1} \equiv \tilde{\mathbf{Q}}_0(z) \leftrightarrow m(z) \mathbf{I}_n$ and the random vector $\boldsymbol{\psi} \in \mathbb{R}^n$ with its i -th entries given by

$$[\boldsymbol{\psi}]_i = \frac{1}{\sqrt{p}} (\|\mathbf{z}_i\|^2 - \mathbb{E}[\|\mathbf{z}_i\|^2]) = \frac{1}{\sqrt{p}} (\|\mathbf{z}_i\|^2 - p).$$

Consider now the informative-plus-noise model \mathbf{K} for $\mathbf{X} = \mathbf{Z} + \boldsymbol{\mu} \mathbf{v}^\top$ as in (15) with $[\mathbf{v}]_i = \pm 1$ and $\|\mathbf{v}\| = \sqrt{n}$. It follows from (Liao & Couillet, 2019) that

$$\left\| \mathbf{K} - \mathbf{K}_0 - \frac{a_1}{p} \begin{bmatrix} \mathbf{v} & \mathbf{Z}^\top \boldsymbol{\mu} \end{bmatrix} \begin{bmatrix} \|\boldsymbol{\mu}\|^2 & 1 \\ 1 & 0 \end{bmatrix} \begin{bmatrix} \mathbf{v}^\top \\ \boldsymbol{\mu}^\top \mathbf{Z} \end{bmatrix} \right\| \rightarrow 0, \quad (23)$$

almost surely as $n, p \rightarrow \infty$.

Combining (22) with (23), we obtain $\|\mathbf{K} - \tilde{\mathbf{K}}_0 - \mathbf{U} \boldsymbol{\Lambda} \mathbf{U}^\top\| \rightarrow 0$ almost surely as $n, p \rightarrow \infty$, with

$$\mathbf{U} = \frac{1}{\sqrt{p}} [\mathbf{1}_n, \mathbf{v}, \boldsymbol{\psi}, \mathbf{Z}^\top \boldsymbol{\mu}] \in \mathbb{R}^{n \times 4}, \quad \boldsymbol{\Lambda} = \begin{bmatrix} 0 & 0 & \frac{a_2}{\sqrt{2}} & 0 \\ 0 & a_1 \|\boldsymbol{\mu}\|^2 & 0 & a_1 \\ \frac{a_2}{\sqrt{2}} & 0 & 0 & 0 \\ 0 & a_1 & 0 & 0 \end{bmatrix} \quad (24)$$

and $(\tilde{\mathbf{K}}_0 - z \mathbf{I}_n)^{-1} \equiv \tilde{\mathbf{Q}}_0(z) \leftrightarrow m(z) \mathbf{I}_n$. By the Woodbury identity, we write

$$\begin{aligned} \mathbf{Q} &= (\mathbf{K} - z \mathbf{I}_n)^{-1} = (\tilde{\mathbf{K}}_0 + \mathbf{U} \boldsymbol{\Lambda} \mathbf{U}^\top - z \mathbf{I}_n)^{-1} + o_{\|\cdot\|}(1) \\ &= \tilde{\mathbf{Q}}_0 - \tilde{\mathbf{Q}}_0 \mathbf{U} (\boldsymbol{\Lambda}^{-1} + \mathbf{U}^\top \tilde{\mathbf{Q}}_0 \mathbf{U})^{-1} \mathbf{U}^\top \tilde{\mathbf{Q}}_0 + o_{\|\cdot\|}(1) \end{aligned} \quad (25)$$

with

$$\boldsymbol{\Lambda}^{-1} + \mathbf{U}^\top \tilde{\mathbf{Q}}_0 \mathbf{U} = \begin{bmatrix} \frac{m(z)}{c} & \frac{m(z)}{c} \frac{\mathbf{v}^\top \mathbf{1}_n}{n} & 0 & 0 \\ \frac{m(z)}{c} \frac{\mathbf{v}^\top \mathbf{1}_n}{n} & \frac{m(z)}{c} & 0 & 0 \\ 0 & 0 & (\kappa - 1) \frac{m(z)}{c} & 0 \\ 0 & 0 & 0 & \boldsymbol{\mu}^\top (\frac{1}{p} \mathbb{E}[\mathbf{Z} \tilde{\mathbf{Q}}_0 \mathbf{Z}^\top]) \boldsymbol{\mu} \end{bmatrix} + o_{\|\cdot\|}(1)$$

where we use the fact that

$$\mathbb{E}[\boldsymbol{\psi}] = \mathbf{0}, \quad \mathbb{E}[\boldsymbol{\psi} \boldsymbol{\psi}^\top] = (\kappa - 1) \mathbf{I}_n.$$

We need to evaluate the expectation $\frac{1}{p} \mathbb{E}[\mathbf{Z} (\tilde{\mathbf{K}}_0 - z \mathbf{I}_n)^{-1} \mathbf{Z}^\top]$. This is given in the following lemma.

Lemma 1. *Under the assumptions and notations of Theorem 1, we have*

$$\frac{1}{p} \mathbb{E}[\mathbf{Z} (\tilde{\mathbf{K}}_0 - z \mathbf{I}_n)^{-1} \mathbf{Z}^\top] = \frac{m(z)}{c + a_1 m(z)} \mathbf{I}_p + o_{\|\cdot\|}(1). \quad (26)$$

Proof of Lemma 1. For $\tilde{\mathbf{Q}}_0 = (\tilde{\mathbf{K}}_0 - z\mathbf{I}_n)^{-1}$, we aim to approximate the expectation $\mathbb{E}[\mathbf{Z}\tilde{\mathbf{Q}}_0\mathbf{Z}^\top]$. Consider first the case where the entries of \mathbf{Z} are i.i.d. Gaussian, we can write the (i, i') entry of $\mathbb{E}[\mathbf{Z}\tilde{\mathbf{Q}}_0\mathbf{Z}^\top]$ with Stein's lemma (i.e., $\mathbb{E}[xf(x)] = \mathbb{E}[f'(x)]$ for $x \sim \mathcal{N}(0, 1)$) as

$$\begin{aligned}\mathbb{E}[\mathbf{Z}\tilde{\mathbf{Q}}_0\mathbf{Z}^\top]_{ii'} &= \sum_{j=1}^n \mathbb{E}[\mathbf{Z}_{ij}[\tilde{\mathbf{Q}}_0\mathbf{Z}^\top]_{ji'}] = \sum_{j=1}^n \mathbb{E}\left[\frac{\partial[\tilde{\mathbf{Q}}_0\mathbf{Z}^\top]_{ji'}}{\partial \mathbf{Z}_{ij}}\right] \\ &= \sum_{j=1}^n \mathbb{E}\left[[\tilde{\mathbf{Q}}_0]_{jj}\delta_{ii'} + \sum_{k=1}^n \frac{\partial[\tilde{\mathbf{Q}}_0]_{jk}}{\partial \mathbf{Z}_{ij}}\mathbf{Z}_{ki'}^\top\right].\end{aligned}$$

We first focus on the term $\frac{\partial[\tilde{\mathbf{Q}}_0]_{jk}}{\partial \mathbf{Z}_{ij}}$ as

$$\frac{\partial[\tilde{\mathbf{Q}}_0]_{jk}}{\partial \mathbf{Z}_{ij}} = -\left[\tilde{\mathbf{Q}}_0 \frac{\partial \mathbf{K}_0}{\partial \mathbf{Z}_{ij}} \tilde{\mathbf{Q}}_0\right]_{jk} = \sum_{l,m=1}^n -[\tilde{\mathbf{Q}}_0]_{jl} \frac{\partial[\mathbf{K}_0]_{lm}}{\partial \mathbf{Z}_{ij}} [\tilde{\mathbf{Q}}_0]_{mk}$$

where we recall $[\mathbf{K}_0]_{ij} = \delta_{i \neq j} f(\mathbf{Z}^\top \mathbf{Z} / \sqrt{p})_{ij} / \sqrt{p}$ so that for $l \neq m$ we have

$$\frac{\partial[\mathbf{K}_0]_{lm}}{\partial \mathbf{Z}_{ij}} = \frac{1}{p} f'(\mathbf{Z}^\top \mathbf{Z} / \sqrt{p})_{lm} \frac{\partial[\mathbf{Z}^\top \mathbf{Z}]_{lm}}{\partial \mathbf{Z}_{ij}} = \frac{1}{p} f'(\mathbf{Z}^\top \mathbf{Z} / \sqrt{p})_{lm} (\delta_{jl} \mathbf{Z}_{im} + \mathbf{Z}_{li}^\top \delta_{jm})$$

and $\frac{\partial[\mathbf{K}_0]_{lm}}{\partial \mathbf{Z}_{ij}} = 0$ for $l = m$. We get

$$\begin{aligned}\sum_{j,k} \frac{\partial[\tilde{\mathbf{Q}}_0]_{jk}}{\partial \mathbf{Z}_{ij}} \mathbf{Z}_{ki'}^\top &= -\frac{1}{p} \sum_{j,k,m} [\tilde{\mathbf{Q}}_0]_{jj} f'(\mathbf{Z}^\top \mathbf{Z} / \sqrt{p})_{jm} \mathbf{Z}_{im} [\tilde{\mathbf{Q}}_0]_{mk} \mathbf{Z}_{ki'}^\top - \frac{1}{p} \sum_{j,k,l} [\tilde{\mathbf{Q}}_0]_{jl} f'(\mathbf{Z}^\top \mathbf{Z} / \sqrt{p})_{lj} \mathbf{Z}_{li}^\top [\tilde{\mathbf{Q}}_0]_{jk} \mathbf{Z}_{ki'}^\top \\ &= -\frac{1}{p} [\mathbf{Z} \text{diag}(f'(\mathbf{Z}^\top \mathbf{Z} / \sqrt{p}) \tilde{\mathbf{Q}}_0 \mathbf{1}_n) \tilde{\mathbf{Q}}_0 \mathbf{Z}^\top]_{ii'} - \frac{1}{p} [\mathbf{Z}(\tilde{\mathbf{Q}}_0 \odot f'(\mathbf{Z}^\top \mathbf{Z} / \sqrt{p})) \tilde{\mathbf{Q}}_0 \mathbf{Z}^\top]_{ii'}\end{aligned}$$

where $f'(\mathbf{Z}^\top \mathbf{Z} / \sqrt{p})$ indeed represents $f'(\mathbf{Z}^\top \mathbf{Z} / \sqrt{p}) - \text{diag}(\cdot)$ in both cases.

For the first term, since $f'(\mathbf{Z}^\top \mathbf{Z} / \sqrt{p}) - \text{diag}(\cdot) = a_1 \mathbf{1}_n \mathbf{1}_n^\top + O_{\|\cdot\|}(\sqrt{p})$, we have

$$\frac{1}{p} f'(\mathbf{Z}^\top \mathbf{Z} / \sqrt{p}) \tilde{\mathbf{Q}}_0 \mathbf{1}_n = \frac{a_1}{p} \mathbf{1}_n^\top \tilde{\mathbf{Q}}_0 \mathbf{1}_n \cdot \mathbf{1}_n + O(p^{-1/2}) = \frac{a_1 m(z)}{c} \mathbf{1}_n + O(p^{-1/2}) \quad (27)$$

where $O(p^{-1/2})$ is understood entry-wise. As a result,

$$\frac{1}{p} \mathbf{Z} \text{diag}(f'(\mathbf{Z}^\top \mathbf{Z} / \sqrt{p}) \tilde{\mathbf{Q}}_0 \mathbf{1}_n) \tilde{\mathbf{Q}}_0 \mathbf{Z}^\top = \frac{a_1 m(z)}{c} \cdot \frac{1}{p} \mathbf{Z} \tilde{\mathbf{Q}}_0 \mathbf{Z}^\top + o_{\|\cdot\|}(1).$$

For the second term, since $f'(\mathbf{Z}^\top \mathbf{Z} / \sqrt{p})$ has $O(1)$ entries and $\|\mathbf{A} \odot \mathbf{B}\| \leq \sqrt{n} \|\mathbf{A}\|_\infty \|\mathbf{B}\|$ for $\mathbf{A}, \mathbf{B} \in \mathbb{R}^{n \times n}$, we deduce that

$$\frac{1}{p} \|\mathbf{Z}(\tilde{\mathbf{Q}}_0 \odot f'(\mathbf{Z}^\top \mathbf{Z} / \sqrt{p})) \tilde{\mathbf{Q}}_0 \mathbf{Z}^\top\| = O(\sqrt{p}).$$

As a consequence, we conclude that

$$\frac{1}{p} \mathbb{E}[\mathbf{Z} \tilde{\mathbf{Q}}_0 \mathbf{Z}^\top] = \frac{1}{p} \text{tr} \tilde{\mathbf{Q}}_0 \cdot \mathbf{I}_p - \frac{a_1 m(z)}{c} \cdot \frac{1}{p} \mathbb{E}[\mathbf{Z} \tilde{\mathbf{Q}}_0 \mathbf{Z}^\top] + o_{\|\cdot\|}(1)$$

that is

$$\frac{1}{p} \mathbb{E}[\mathbf{Z} \tilde{\mathbf{Q}}_0 \mathbf{Z}^\top] = \frac{m(z)}{c + a_1 m(z)} \mathbf{I}_p + o_{\|\cdot\|}(1)$$

where we recall $\text{tr} \tilde{\mathbf{Q}}_0 / p = m(z)/c$ and thus the conclusion of Lemma 1 for the Gaussian case. The interpolation trick (Lytova & Pastur, 2009, Corollaray 3.1) can be applied to extend the result beyond Gaussian distribution. This concludes the proof of Lemma 1. \square

With Lemma 1 and denoting the shortcut $\mathbf{A} = (\mathbf{\Lambda}^{-1} + \mathbf{U}^\top \tilde{\mathbf{Q}}_0 \mathbf{U})^{-1}$, we have

$$\begin{aligned} \mathbb{E}[\mathbf{U}\mathbf{A}\mathbf{U}^\top] &= \frac{1}{p}(\mathbf{A}_{11}\mathbf{1}_n\mathbf{1}_n^\top + \mathbf{A}_{12}\mathbf{1}_n\mathbf{v}^\top + \mathbf{A}_{21}\mathbf{v}\mathbf{1}_n^\top + \mathbf{A}_{22}\mathbf{v}\mathbf{v}^\top + \mathbf{A}_{33}(\kappa - 1)\mathbf{I}_n + \mathbf{A}_{44}\|\boldsymbol{\mu}\|^2\mathbf{I}_n) \\ &= \frac{1}{p}(\mathbf{A}_{11}\mathbf{1}_n\mathbf{1}_n^\top + \mathbf{A}_{12}\mathbf{1}_n\mathbf{v}^\top + \mathbf{A}_{21}\mathbf{v}\mathbf{1}_n^\top + \mathbf{A}_{22}\mathbf{v}\mathbf{v}^\top) + o_{\|\cdot\|}(1) \end{aligned}$$

since $\|\boldsymbol{\mu}\| = O(1)$ and $\|\mathbf{v}\| = O(\sqrt{n})$. We thus deduce from (25) that

$$\mathbf{Q}(z) \leftrightarrow \bar{\mathbf{Q}}(z) = m(z)\mathbf{I}_n - cm^2(z)\mathbf{V} \begin{bmatrix} \mathbf{A}_{11} & \mathbf{A}_{12} \\ \mathbf{A}_{21} & \mathbf{A}_{22} \end{bmatrix} \mathbf{V}^\top$$

with $\sqrt{n}\mathbf{V} = [\mathbf{v}, \mathbf{1}_n]$. Rearranging the expression we conclude the proof of Theorem 1.

A.2 Proof of Corollary 1 and related discussions

Consider the noise-only model by taking $\boldsymbol{\mu} = \mathbf{0}$ in Theorem 1. Then, we have $\mathbf{K} = \mathbf{K}_0$ and $\Theta(z) = 0$, so that

$$\bar{\mathbf{Q}}(z) = m(z) + \Omega(z) \cdot \frac{1}{n}\mathbf{1}_n\mathbf{1}_n^\top, \quad \Omega(z) = \frac{a_2^2(\kappa - 1)m^3(z)}{2c^2 - a_2^2(\kappa - 1)m^2(z)} \quad (28)$$

where we recall $m(z)$ is the solution to

$$m(z) = - \left(z + \frac{a_1^2 m(z)}{c + a_1 m(z)} + \frac{\nu - a_1^2}{c} m(z) \right)^{-1}. \quad (29)$$

Since the resolvent $\mathbf{Q}(z)$ is undefined for $z \in \mathbb{R}$ within the eigensupport of \mathbf{K} that consists of (i) the main bulk characterized by the Stieltjes transform $m(z)$ defined in (29) and (ii) the possible spikes, we need to find the poles of $\mathbf{Q}(z)$ but not those of $m(z)$ to determine the asymptotic locations of the spikes that are *away from* the main bulk. Direct calculations show that the Stieltjes transforms of the possible *non-informative* spikes satisfy

$$m_\pm = \pm \sqrt{\frac{2}{\kappa - 1} \frac{c}{a_2}} \quad (30)$$

that are in fact the poles of $\Omega(z)$, for $a_2 \neq 0$ and $\kappa \neq 1$. For $\kappa = 1$ or $a_2 = 0$, $\Omega(z)$ has no (additional) poles, so that there is almost surely no spike outside the limiting spectrum.

It is however not guaranteed that $z \in \mathbb{R}$ corresponding to (30) isolates from the main bulk. To this end, we introduce the following characterization of the limiting measure in (29).

Corollary 3 (Limiting spectrum). *Under the notations and conditions of Theorem 1, with probability one, the empirical spectral measure $\omega_n = \frac{1}{n} \sum_{i=1}^n \delta_{\lambda_i(\mathbf{K}_0)}$ of the noise-only model \mathbf{K}_0 (and therefore that of \mathbf{K} as a low rank additive perturbation of \mathbf{K}_0 via (23)) converges weakly to a probability measure ω of compact support as $n, p \rightarrow \infty$, with ω uniquely defined through its Stieltjes transform $m(z)$ solution to (29). Moreover,*

1. if we let $\text{supp}(\omega)$ be the support of ω , then

$$\text{supp}(\omega) \cup \{0\} = \mathbb{R} \setminus \{x(m) \mid m \in \mathbb{R} \setminus \{-c/a_1\} \cup \{0\}\} \text{ and } x'(m) > 0\} \quad (31)$$

for $x(m)$ the functional inverse of (29) explicitly given by

$$x(m) = -\frac{1}{m} - \frac{a_1^2 m}{c + a_1 m} - \frac{\nu - a_1^2}{c} m, \quad (32)$$

2. the measure ω has a density and its support may have up to four edges, with the associated Stieltjes transforms m s given by the roots of $x'(m) = 0$, i.e.,

$$x'(m) = \frac{1}{m^2} - \frac{a_1^2 c}{(c + a_1 m)^2} - \frac{\nu - a_1^2}{c} = 0. \quad (33)$$

The limiting spectral measure ω of the null model \mathbf{K}_0 was first derived in (Cheng & Singer, 2013) for Gaussian distribution and then extended to sub-exponential distribution in (Do & Vu, 2013). The fact that a finite rank perturbation does not affect the limiting spectrum follows from (Silverstein & Bai, 1995, Lemma 2.6).

The characterization in (31) above follows the idea in (Silverstein & Choi, 1995, Theorem 1.1), which arises from the crucial fact that the Stieltjes transform $m(x) = \int (t - x)^{-1} \omega(dt)$ of a measure ω is an increasing function on its domain of definition and so must be its functional inverse $x(m)$ given in (32). In plain words, Corollary 3 tell us that (i) depending on the number of real solutions to (33), the support of ω may contain two disjoint regions with four edges, and (ii) $x \in \mathbb{R}$ is outside the support of ω if and only if its associated Stieltjes transform m satisfies $x'(m) > 0$, i.e., belonging to the increasing region the functional inverse $x(m)$ in (32). This is depicted in Figure 8, where for the same function $f(t) = \max(t, 0) - 1/\sqrt{2\pi}$ with $a_1 = 1/2$, $a_2 = 1/(2\sqrt{\pi})$ and $\nu = (\pi - 1)/(2\pi)$, we observe in the top display a single region of ω for $c = 2$ and in the bottom display two disjoint regions (with thus four edges) for $c = 1/10$. The corresponding empirical eigenvalue histograms and limiting laws are given in Figure 9. Note, in particular, that the local extrema of the functional inverse $x(m)$ in Figure 8 characterize the (possibly up to four) edges of the support of ω in Figure 9.

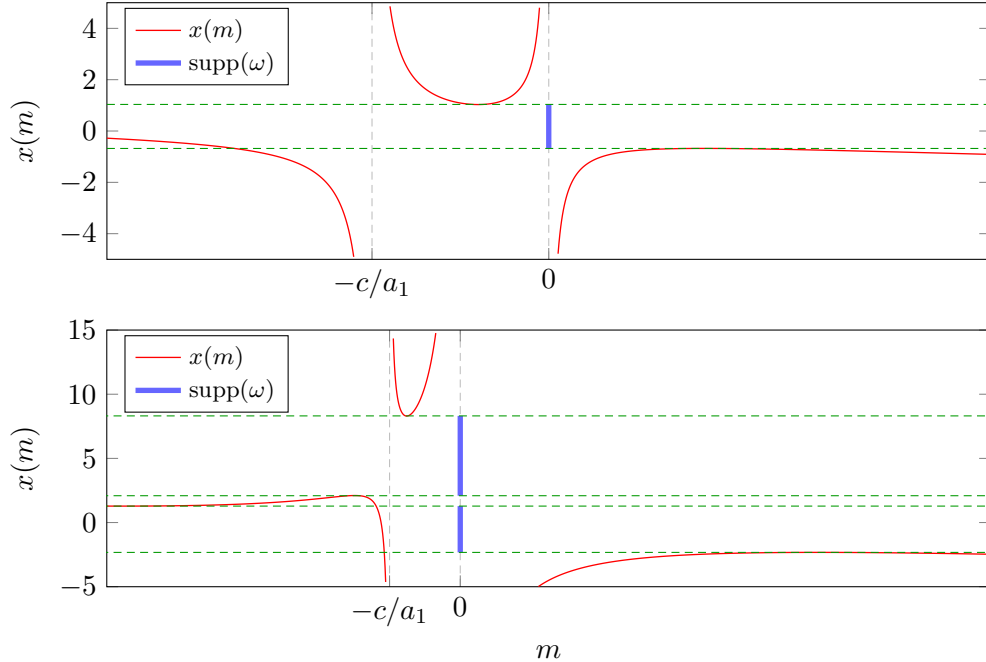


Figure 8: Functional inverse $x(m)$ for $m \in \mathbb{R} \setminus \{-c/a_1\} \cup \{0\}$, with $f(t) = \max(t, 0) - 1/\sqrt{2\pi}$, for $c = 2$ (**above**, with two edges) and $c = 1/10$ (**bottom**, with four edges). The support of ω can be read on the vertical axes and the values of x such that $x'(m) = 0$ are marked in **green**.

According to the discussion above, it remains to check the sign of $x'(m)$ for $m = \pm \sqrt{\frac{2}{\kappa-1} \frac{c}{a_2}}$ to see if they correspond to isolated eigenvalues away from the support of ω . This, after some algebraic manipulations, concludes the proof of Corollary 1.

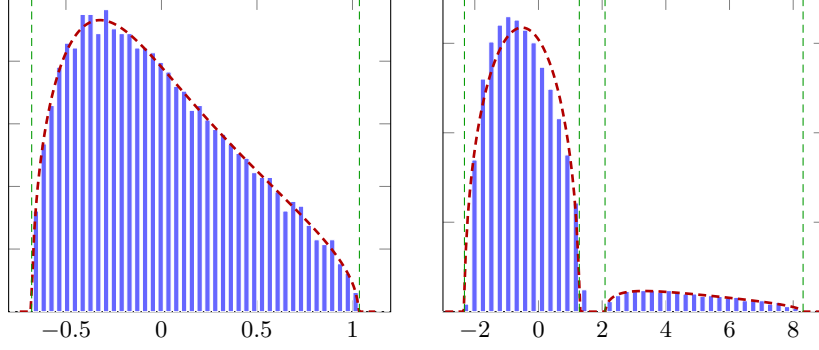


Figure 9: Eigenvalues of \mathbf{K} with $\mu = \mathbf{0}$ (blue) versus the limiting laws in Theorem 1 and Corollary 3 (red) for $p = 3\,200$, $n = 1\,600$ (left) and $p = 400$, $n = 4\,000$ (right), with $f(t) = \max(t, 0) - 1/\sqrt{2\pi}$ and Gaussian data. The values of x such that $x'(m) = 0$ in Figure 8 are marked in green.

Discussions. The limiting spectral measure in Corollary 3 can be shown to be a “mix” between the popular Marčenko-Pastur and the Wigner’s semicircle law.

Remark 2 (From Marčenko-Pastur to semicircle law). *As already pointed out (Fan & Montanari, 2019), here the limiting spectral measure ω is the so-called free additive convolution (Voiculescu, 1986) of the semicircle and Marčenko-Pastur laws, weighted respectively by a_1 and $\sqrt{\nu - a_1^2}$, i.e.,*

$$\omega = a_1(\omega_{MP,c^{-1}} - 1) \boxplus \sqrt{(\nu - a_1^2)/c} \cdot \omega_{SC} \quad (34)$$

where we denote $a_1(\omega_{MP,c^{-1}} - 1)$ the law of $a_1(x - 1)$ for $x \sim \omega_{MP,c^{-1}}$ and $\sqrt{(\nu - a_1^2)/c} \cdot \omega_{SC}$ the law of $\sqrt{(\nu - a_1^2)/c} \cdot x$ for $x \sim \omega_{SC}$. Figure 10 compares the eigenvalue distributions of \mathbf{K}_0 for $f(t) = a_1 t + a_2(t^2 - 1)/\sqrt{2}$ (so that $\nu - a_1^2 = a_2^2$) with different pairs of (a_1, a_2) . We observe a transition from the Marčenko-Pastur law (in the left display, with $a_1 \neq 0$ and $a_2 = 0$) to the semicircle law (in the right display, with $a_1 = 0$ and $a_2 \neq 0$).

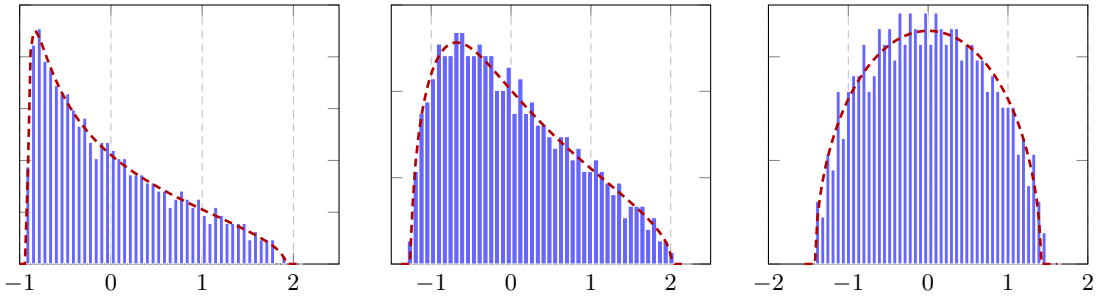


Figure 10: Eigenvalues of \mathbf{K} with $\mu = \mathbf{0}$ (blue) versus the limiting laws in Theorem 1 and Corollary 3 (red) for Gaussian data, $p = 1\,024$, $n = 512$ and $f(t) = a_1 t + a_2(t^2 - 1)/\sqrt{2}$ with $a_1 = 1, a_2 = 0$ (left), $a_1 = 1, a_2 = 1/2$ (middle), and $a_1 = 0, a_2 = 1$ (right).

Remark 2 tells us that, depending on the ratio ν/a_1^2 , the eigenspectrum of \mathbf{K} exhibits a transition from the Marčenko-Pastur to semicircle-like shape. Note from Figure 1-(right) that, for the sparse f_1 , the ratio ν/a_1^2 is an increasing function of the truncation threshold s and therefore, as the matrix \mathbf{K} become sparser, its eigenspectrum changes from a Marčenko-Pastur-type (at $s = 0$) to be more

semicircle-like. This is depicted in Figure 11 and similar conclusions hold for quantized f_2 and binary f_3 in the $s \geq s_{\text{opt}}$ regime.

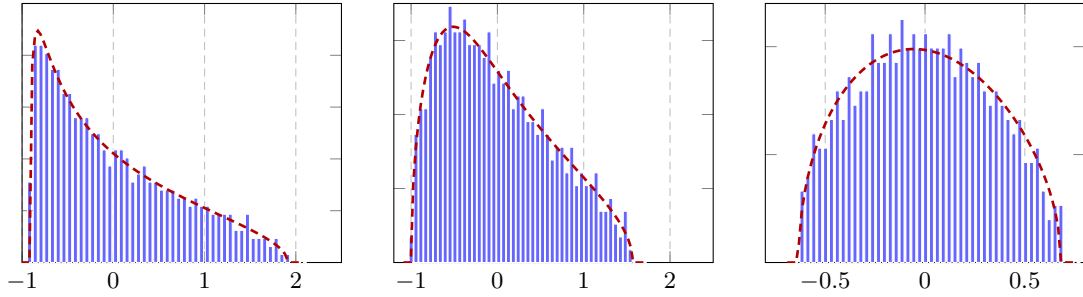


Figure 11: Eigenvalues of \mathbf{K} with $\mu = \mathbf{0}$ (blue) versus the limiting laws in Theorem 1 and Corollary 3 (red) for Gaussian data, $p = 1024$, $n = 512$ and $f(t) = t \cdot 1_{|t| > \sqrt{2}s}$ with $s = 0.1$ (left), $s = .75$ (middle), and $s = 1.5$ (right).

As discussed after Theorem 1 and in the proof above, while the limiting eigenvalue distribution ω is *universal* and *independent* of the law of the entries of \mathbf{Z} , so long as they are independent, sub-exponential, of zero mean and unit variance, as commonly observed in RMT (Tao et al., 2010), this is no longer the case for the isolated eigenvalues. In particular, according to Corollary 1, the possible non-informative spikes *depend* on the kurtosis κ of the distribution. In Figure 12 we observe a farther (left) spike for Student-t (with $\kappa = 5$) than Gaussian distribution (with $\kappa = 3$), while *no* spike can be observed for the symmetric Bernoulli distribution (that takes values ± 1 with probability $1/2$ so that $\kappa = 1$), with the same limiting eigenvalue distribution for $f(t) = \max(t, 0) - 1/\sqrt{2\pi}$.

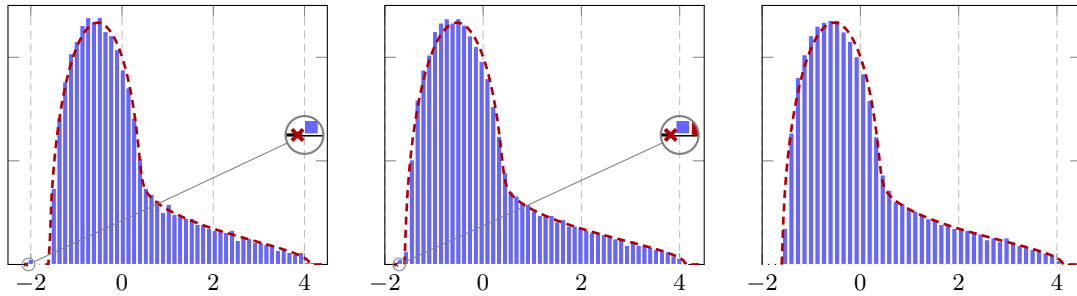


Figure 12: Eigenvalues of \mathbf{K} with $\mu = \mathbf{0}$ (blue) versus the limiting laws and spikes in Theorem 1 and Corollary 1 (red) for Student-t (with 7 degrees of freedom, left), Gaussian (middle) and Rademacher distribution (right), $p = 512$, $n = 2048$, $f(t) = \max(t, 0) - 1/\sqrt{2\pi}$, with an emphasis on the *non-informative* spikes at *different* locations: at -2.10 for Student-t and -1.77 for Gaussian.

Remark 3 (Non-informative spike in-between). *When the support of ω consists of two disjoint regions (e.g., in the right plot of Figure 9), a non-informative spike may appear between these two regions, that corresponds to such an $m < -c/a_1$ in the setting of Figure 8-(bottom), when $a_1\sqrt{\frac{2}{\kappa-1}} > a_2$. An example is provided in Figure 13.*

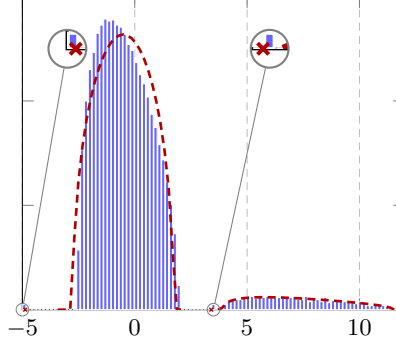


Figure 13: Eigenvalues of \mathbf{K} with $\boldsymbol{\mu} = \mathbf{0}$ (blue) versus the limiting laws and spikes in Corollary 3 and 1 (red) for $p = 400$, $n = 6000$, with $f(t) = \max(t, 0) - 1/\sqrt{2\pi}$ and Gaussian data.

A.3 Proof of Corollary 2 and related discussions

Similar to our discussions in Section A.2, we need to find the poles of $\det \boldsymbol{\Lambda}(z)$, that are real solutions to $H(x) = 0$ with

$$H(x) = a_1 a_2^2 (\kappa - 1) \left(\frac{(\mathbf{v}^\top \mathbf{1}_n)^2}{n^2} \rho - 1 - \rho \right) m^3(x) - a_2^2 c (\kappa - 1) m^2(x) + 2a_1 c^2 (\rho + 1) m(x) + 2c^3 = 0 \quad (35)$$

for $m(z)$ the unique solution to (9) and $\rho = \lim_p \|\boldsymbol{\mu}\|^2$. Note that

1. for $a_1 a_2^2 (\kappa - 1) \left(\frac{(\mathbf{v}^\top \mathbf{1}_n)^2}{n^2} \rho - 1 - \rho \right) \neq 0$, there can be (up to) three spikes;
2. with $a_1 = 0$ and $a_2 \neq 0$, we get $m^2(x) = \frac{2c^2}{a_2^2 (\kappa - 1)}$ and there are at most two spikes: this is equivalent to the case of Corollary 1 with $\rho = 0$; in fact, taking a_1 we *discard* the information in the signal $\boldsymbol{\mu}$, as pointed out in (Liao & Couillet, 2019);
3. with $a_2 = 0$ and $a_1 \neq 0$ we obtain $m(x) = -\frac{c}{a_1 (\rho + 1)}$, this is the case of Corollary 2.

For a given isolated eigenvalue-eigenvector pair $(\hat{\lambda}, \hat{\mathbf{v}})$ (assumed to be of multiplicity one), the projection $|\hat{\mathbf{v}}^\top \mathbf{v}|^2$ onto the data label vector \mathbf{v} can be evaluated via the Cauchy's integral formula and our Theorem 1. More precisely, consider a positively oriented contour Γ that circles around *only* the isolated $\hat{\lambda}$, we write

$$\begin{aligned} \frac{1}{n} \mathbf{v}^\top \hat{\mathbf{v}} \hat{\mathbf{v}}^\top \mathbf{v} &= -\frac{1}{2\pi i} \oint_{\Gamma} \frac{1}{n} \mathbf{v}^\top (\mathbf{K} - z \mathbf{I}_n)^{-1} \mathbf{v} dz \\ &= -\frac{1}{2\pi i} \oint_{\Gamma} \frac{1}{n} \mathbf{v}^\top (m(z) \mathbf{I}_n - \mathbf{V} \boldsymbol{\Lambda}(z) \mathbf{V}^\top) \mathbf{v} dz + o(1) \\ &= \frac{1}{n} \mathbf{v}^\top \mathbf{V} \left(\frac{1}{2\pi i} \oint_{\Gamma} \boldsymbol{\Lambda}(z) dz \right) \mathbf{V}^\top \mathbf{v} + o(1) = \frac{1}{n} \mathbf{v}^\top \mathbf{V} (\text{Res} \boldsymbol{\Lambda}(z)) \mathbf{V}^\top \mathbf{v} + o(1) \\ &= \begin{bmatrix} 1 & \frac{\mathbf{v}^\top \mathbf{1}_n}{n} \end{bmatrix} \left(\lim_{z \rightarrow \hat{\lambda}} (z - \lambda) \begin{bmatrix} \Theta(z) m^2(z) & \Theta(z) \Omega(z) \frac{\mathbf{v}^\top \mathbf{1}_n}{n} m(z) \\ \Theta(z) \Omega(z) \frac{\mathbf{v}^\top \mathbf{1}_n}{n} m(z) & \Theta(z) \Omega^2(z) \frac{(\mathbf{v}^\top \mathbf{1}_n)^2}{n^2} - \Omega(z) \end{bmatrix} \right) \begin{bmatrix} 1 \\ \frac{\mathbf{v}^\top \mathbf{1}_n}{n} \end{bmatrix} + o(1) \end{aligned}$$

where we use Theorem 1 for the second line and recall that the asymptotic location λ of $\hat{\lambda}$ is away from the support of limiting spectral measure ω so that $-\frac{1}{2\pi i} \oint_{\Gamma} m(z) dz = 0$ in the third line.

Interestingly, we note at this stage that taking $\mathbf{v}^\top \mathbf{1}_n = o(n)$ or $a_2 = 0$ (so that $\Omega(z) = 0$) leads to the following simplification

$$\frac{1}{n} |\mathbf{v}^\top \hat{\mathbf{v}}|^2 = \lim_{z \rightarrow \lambda} (z - \lambda) \Theta(z) m^2(z) + o(1) = \lim_{z \rightarrow \lambda} (z - \lambda) \frac{a_1 \rho m^2(z)}{c + a_1 m(z)(1 + \rho)} + o(1) \quad (36)$$

$$= \frac{a_1 \rho}{1 + \rho} \frac{m^2(\lambda)}{m'(\lambda)} + o(1) = \frac{a_1 \rho}{1 + \rho} \left(1 - \frac{a_1^2 c m^2(\lambda)}{(c + a_1 m(\lambda))^2} - \frac{\nu - a_1^2}{c} m^2(\lambda) \right) + o(1) \quad (37)$$

with l'Hospital's rule and the fact that $m'(z) = \left(\frac{1}{m^2(z)} - \frac{a_1^2 c}{(c + a_1 m(z))^2} - \frac{\nu - a_1^2}{c} \right)^{-1}$ from (9).

In particular, in the setting of Corollary 2 with $a_1 > 0$ and $a_2 = 0$, with the substitution $m(\lambda) = m_\rho = -\frac{c}{a_1(\rho+1)}$ into (37) and then the change of variable $m = -\frac{c}{a_1} \frac{1}{1+x}$, we obtain the expression of $F(x)$ in Corollary 2. The phase transition condition can be similarly obtained, as discussed in Section A.2, by checking the sign of the derivative of the functional inverse $x'(m)$ as for Corollary 3. This concludes the proof of Corollary 2.

Discussions. Note that, while with either $a_2 = 0$ or $\mathbf{v}^\top \mathbf{1}_n = o(n)$ we obtain the same expression for the projection $|\mathbf{v}^\top \hat{\mathbf{v}}|^2$, the possible spike of interest $\hat{\lambda}$ (and its asymptotic location λ) in these two scenarios can be rather different. More precisely,

1. with $a_2 = 0$, there is a single possible spike $\hat{\lambda}$ with $m(\lambda) = m_\rho = -\frac{c}{a_1(\rho+1)}$;
2. with $\mathbf{v}^\top \mathbf{1}_n = o(n)$, there can be up to three spikes that correspond to $m_\rho = -\frac{c}{a_1(\rho+1)}$ and $m_\pm = \pm \frac{c}{a_2} \sqrt{\frac{2}{\kappa-1}}$.

This observation leads to the following remark.

Remark 4 (Noisy top eigenvector with $a_2 \neq 0$). For $\mathbf{v}^\top \mathbf{1}_n = o(n)$ and $a_2 \neq 0$, one may have $m_- = -\frac{c}{a_2} \sqrt{\frac{2}{\kappa-1}} > -\frac{c}{a_1(\rho+1)} = m_\rho$ for instance with large a_2 and small a_1 . Since $m(x)$ is an increasing function, the top eigenvalue-eigenvector pair of \mathbf{K} can be non-informative, independent of the SNR ρ , and totally useless for clustering purposes. An example is provided in Figure 2 where one observes that (i) the largest spike (on the right-hand side) corresponds to a noisy eigenvector while the second largest spike contains the data class-structure \mathbf{v} ; and (ii) the theoretical prediction of the eigen-alignment α in Corollary 2 still holds here due to $\mathbf{v}^\top \mathbf{1}_n = o(n)$. This extends our Corollary 1 to the signal-plus-noise scenario and confirms the advantage and necessity of taking $a_2 = 0$.

As a side remark, in contrast to Remark 3 and Figure 13, where we observe that the non-informative spike can be lying between the two disjoint regions of the limiting measure ω , in the case of $a_1 > 0$, the informative spike $m_\rho = -\frac{c}{a_1(\rho+1)}$ can *only* appear on the *right side* of the support of ω , since $-\frac{c}{a_1} < -\frac{c}{a_1(\rho+1)} < 0$ for $\rho = \lim_p \|\boldsymbol{\mu}\|^2 \geq 0$. See Figure 8-(bottom) for an illustration.

A.4 Proof of Proposition 1

Note that, for $\hat{\mathbf{v}}$ the top isolated eigenvector of \mathbf{K} , with Corollary 2 we can write

$$\hat{\mathbf{v}} = \sqrt{\alpha} \mathbf{v} / \sqrt{n} + \sigma \mathbf{w} \quad (38)$$

for some $\sigma \in \mathbb{R}$, $\mathbf{w} \in \mathbb{R}^n$ a zero-mean random vector, orthogonal to \mathbf{v} , and of unit norm. To evaluate the asymptotic clustering performance in the setting of Proposition 1 (i.e., with the estimate $\hat{\mathcal{C}}_i = \text{sign}([\hat{\mathbf{v}}]_i)$ for $\hat{\mathbf{v}}^\top \mathbf{v} \geq 0$), we need to assess the probability $\Pr(\text{sign}([\hat{\mathbf{v}}]_i) < 0)$ for $\mathbf{x}_i \in \mathcal{C}_1$ and

$\Pr(\text{sign}([\hat{\mathbf{v}}]_i) > 0)$ for $\mathbf{x}_i \in \mathcal{C}_2$ (recall that the class-label $[\mathbf{v}]_i = -1$ for $\mathbf{x}_i \in \mathcal{C}_1$ and $[\mathbf{v}]_i = +1$ for $\mathbf{x}_i \in \mathcal{C}_2$), and it thus remains to derive σ . Note that

$$1 = \hat{\mathbf{v}}^\top \hat{\mathbf{v}} = \alpha + 2\sigma\sqrt{\alpha}\mathbf{w}^\top \mathbf{v}/\sqrt{n} + \sigma^2 = \alpha + \sigma^2 + o(1) \quad (39)$$

where we recall $\|\mathbf{v}\| = \sqrt{n}$, which, together with an argument on the normal fluctuations of $\hat{\mathbf{v}}$ (Kadavankandy & Couillet, 2019), concludes the proof.

B Additional empirical results on real-world datasets

In Figure 14, we compare the clustering performance, the level of sparsity, and the computational time of the top eigenvector, of the sparse function f_1 and quantized f_2 with $M = 2$ (so 2 bits per non-zero entry), on the MNIST dataset. We see that, different from the binary f_3 with which small entries of \mathbf{K} are set to zero, the quantized function f_2 , by letting the small entries of \mathbf{K} to take certain *nonzero* values, yields surprisingly good performance on the MNIST dataset. This performance gain comes, however, at the price of somewhat heavy computational burden that is approximately the same as the original dense matrix $\mathbf{X}^\top \mathbf{X}$, since we lose the sparsity with f_2 , see Figure 1-(left).

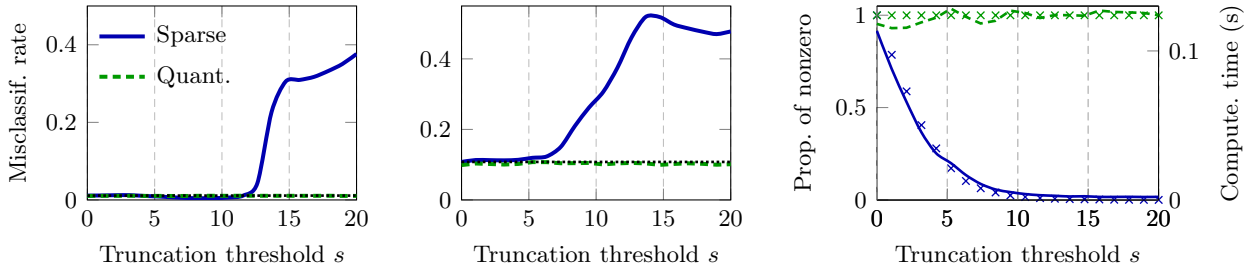


Figure 14: Clustering performance (**left**), proportion of nonzero entries, and computational time of the top eigenvector (**right**, in markers) of sparse f_1 and quantized f_2 with $M = 2$, as a function of the truncation threshold s on the MNIST dataset: digits (0, 1) (**left**) and (5, 6) (**middle and right**) with $n = 2048$ and performance of the linear function in **black**. Results averaged over 100 runs.

Also, from the left and middle displays of Figure 7 and Figure 14, we see that for MNIST data, while the classification error rate on the pair (0, 1) can be as low as 1%, the performances on the pair (5, 6) are far from satisfactory, with the linear $f(t) = t$ and the proposed f_1 , f_2 or f_3 . This is the limitation of the proposed statistical model in (1), which only takes into account the *first order discriminative statistics*. Indeed, it has been shown in (Liao & Couillet, 2019) that, taking $a_2 = 0$ (as in the case of the proposed f_1 , f_2 and f_3) asymptotically discards the *second order discriminative statistics* in the covariance structure, and may thus result in suboptimal performance. It would be of future interest to extend the current analysis to the “generic” Gaussian mixture classification: $\mathcal{N}(\boldsymbol{\mu}_1, \mathbf{C}_1)$ versus $\mathcal{N}(\boldsymbol{\mu}_2, \mathbf{C}_2)$ by considering the impact of (i) asymmetric means $\boldsymbol{\mu}_1$ and $\boldsymbol{\mu}_2$ and (ii) statistical information in the covariance structure \mathbf{C}_1 versus \mathbf{C}_2 and (iii) possibly a K -class mixture model with $K \geq 3$.

In Figure 15, we compare the clustering performances of the proposed f_1 , f_2 , and f_3 on other MNIST-like datasets including the Fashion-MNIST (Xiao et al., 2017), Kuzushiji-MNIST (Clanuwat et al., 2018), and Kannada-MNIST (Prabhu, 2019) datasets. Then, in Figure 16, we compare the performances on the representations of the ImageNet dataset (Deng et al., 2009) from the popular GoogLeNet (Szegedy et al., 2015) of feature dimension $p = 2048$. On various real-world data or features, we made similar observations as in the case of MNIST data as in Figure 7 and Figure 14:

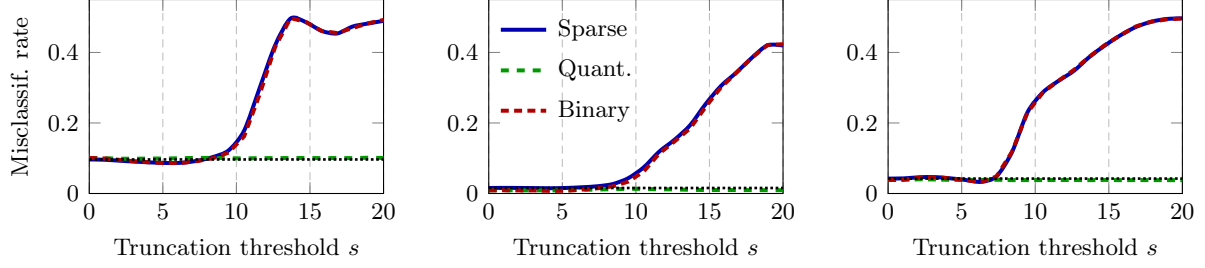


Figure 15: Clustering performance of sparse f_1 , quantized f_2 (with $M = 2$) and binary f_3 as a function of the truncation threshold s on: **(left)** Kuzushiji-MNIST class 3 versus 4, **(middle)** Fashion-MNIST class 0 versus 9, and **(right)** Kannada-MNIST class 4 versus 8, for $n = 2048$ and performance of the linear function in **black**. Results averaged over 100 runs.

the performances of sparse f_1 and binary f_3 are very similar and generally degrade as the threshold s becomes large, while the quantized f_2 yields consistently good performance that is extremely close to that of the linear function. This is in line with the (theoretically sustained) observation in (Seddik et al., 2020) that the “deep” representations of real-world datasets behave, in the large n, p regime, very similar to simple Gaussian mixtures, thereby conveying a strong practical motivation for the present analysis.

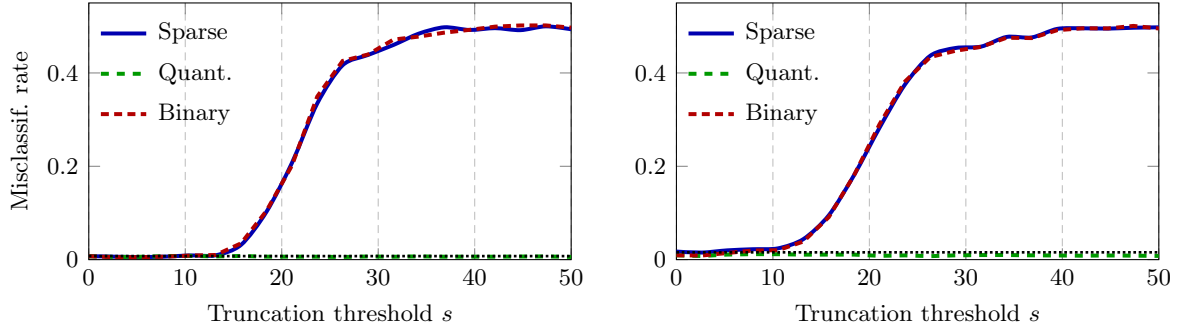


Figure 16: Clustering performance of sparse f_1 , quantized f_2 (with $M = 2$) and binary f_3 as a function of the truncation threshold s on *GoogLeNet* features of the ImageNet datasets: **(left)** class “pizza” versus “daisy” and **(right)** class “hamburger” versus “coffee”, for $n = 1024$ and performance of the linear function in **black**. Results averaged over 10 runs.